A model based on Hirano-Exner equations for two-dimensional transient flows over heterogeneous erodible beds

C. Juez[a,*], C. Ferrer-Boix[b], J. Murillo[a], M. A. Hassan[b], P. García-Navarro[a]

[a] *LIFTEC, CSIC-Universidad de Zaragoza, Spain*
[b] *University of British Columbia, Canada*

Abstract

In order to study the morphological evolution of river beds composed of heterogeneous material, the interaction among the different grain sizes must be taken into account. In this paper, these equations are combined with the two-dimensional shallow water equations to describe the flow field. The resulting system of equations can be solved in two ways: (i) in a coupled way, solving flow and sediment equations simultaneously at a given time-step or (ii) in an uncoupled manner by first solving the flow field and using the magnitudes obtained at each time-step to update the channel morphology (bed and surface composition). The coupled strategy is preferable when dealing with strong and quick interactions between the flow field, the bed evolution and the different particle sizes present on the bed surface. A number of numerical difficulties arise from solving the fully coupled system of equations. These problems are reduced by means of a weakly-coupled strategy to numerically estimate the wave celerities containing the information of the bed and the grain sizes present on the bed. Hence, a two-dimensional numerical scheme able to simulate in a self-stable way the unsteady morphological evolution of channels formed by cohesionless grain size mixtures is presented. The coupling technique is simplified without decreasing the number of waves involved in the numerical scheme but by simplifying their definitions. The numerical results are satisfactorily tested with synthetic cases and against experimental data.

*Corresponding author
Email address: carmelo@unizar.es (C. Juez)

Keywords: 2D Shallow Water Equations, Exner equation, Hirano equation, sorting celerities, heterogeneous material, dynamically chosen time-step

1. Introduction

River morphodynamics refer to the study of the interactions between the bed and the banks of a river and the flow field. The study of these interactions by means of a numerical model requires a set of equations to describe the flow field (e.g. the shallow water equations [1]), and a conservation equation for the mass of sediment, i.e. the Exner equation [2]. If bedload dominates and the sediment concentration is low (less than 1 %, [3]), the classical Exner equation is enough to determine the morphological changes in a river. This approach has been extensively used for the study of one-dimensional ([4, 5, 6, 7]) and two-dimensional (e.g. [8, 9, 10, 11, 12, 13, 14]) morphodynamic problems.

The Exner equation combined with the two-dimensional shallow water equations has been recently extended to sediment mixtures. In these situations, total sediment transport rates are computed as the sum of the contribution from each grain size. Depending on the proportion of each size fraction and the mode by which bed particles are transported, sediment transport rates are estimated through a bed-load or a suspended-load formula [15, 16, 17, 18, 19]. Additionally, imbalances between the actual and the capacity of sediment transport (non-equilibrium sediment transport models) which arise, among other from surface structuring and sorting, have been considered [15, 16, 19]. Hence, temporal and spatial lag effects between the local hydrodynamic conditions and the sediment load are taken into account [20, 21]. However, as recently noted by [11], the uncertainty on some key parameters associated to non-equilibrium models can lead to significant differences on the results.

When a river bed is composed of sediment mixtures, the general Exner equation for the conservation of mass of sediment is not enough to properly describe the morphodynamic evolution of the river. Under these situations, some other equations are needed to assure the conservation of each grain size present on the bed surface. Since particles on the bed might be exchanged with grain sizes on the substrate, a key issue is to evaluate how particles sort vertically from the surface downwards leading to a vertical stratigraphy of the river bed. Vertical sorting thus depends on the fluxes between the different bed layers and the sediment transported on the bed surface. There have been several attempts to evaluate these vertical exchanges [15, 22, 23, 18, 19]. Among them, the most used widely vertical discretization has been the one introduced by [24]. In there, Hirano introduced the presence of a sediment exchange layer, the so called "active layer". This uppermost layer of the bed is assumed to concentrate the interactions between the sediment transport and those fractions of material present on the river bed. Besides, the thickness of the active layer encompasses the fluctuations of the bed elevation at a given point of the bed [25]. Consequently, this layer acts as a buffer in the exchanges between the bedload transport and the substrate which provides a source of sediment to be entrained by the flow, [26, 27, 28].

Steady [17, 29] and unsteady [30, 31, 32, 33, 34, 35, 36, 37, 38, 39] active layers have been assumed by a number of researchers. In both cases, a closure equation is needed to evaluate its thickness. Since the active layer thickness embraces the fluctuations of the bed [25], a physically-based approach is needed to link its value to some reference grain size or to some representative bedform height. Under the hypothesis of one-dimensional and steady flow, the thickness of the active layer has been usually chosen as multiple of the characteristic grain-size on the bed [30, 31, 32, 33, 34, 37, 38], which can vary in time and space.

Letting aside the deformation of the bed and the appearance of bedforms affecting the bed roughness, the temporal variation of the surface composition implies a subsequent variation of the bed friction. This time-varying approach of the bed roughness has been traditionally incorporated in one-dimensional numerical models for mixtures, [31, 32, 33, 34, 36, 37, 38, 39]. However, with the exception of [19] who simulates the evolution of a braided stream and accounts for the variation of both skin and drag friction, few two-dimensional numerical models take time-varying roughness into consideration.

From the numerical point of view, the coupling/uncoupling of the water flow equations with those describing the evolution of the bed has attracted the attention of researchers. [40] displayed that uncoupled strategies were only valid for a narrow range of hydrodynamic regimes governed by low Froude numbers, limiting the velocity at which the bed and the flow field interact with one another. Based on De Vriend's approach, [41] developed a coupled numerical model in which a set of approximate solutions for the bed celerity and sorting celerities, i.e. the speeds at which a perturbation on the surface fractions propagates along the domain, were proposed. However, that approximation was obtained assuming quasi-steady flow. Based on Ribberink's approximation, [42] graphically estimated the celerities of the system for unsteady flows and sediment mixtures composed of only two grain sizes. Additionally, [41] noticed that under certain situations, the Saint-Venant equations in combination with Hirano's equation lead to an elliptic system of equations. This elliptic nature is inconvenient for solving unsteady water flow problems, [29], which are genuinely defined as hyperbolic [43].

In [44], the Hirano model was mixed with the Exner equation for decreasing the number of interrelationships among variables. This theory has been widely implemented in steady 1D numerical schemes [32, 34, 37, 38, 39] and more recently, in a 1D coupled model in [45]. However, this theory has not been included in a pure two-dimensional unsteady numerical scheme.

In the present work, an efficient numerical strategy proposed for uniform grain sizes in [14] is extended to sediment mixtures. For that purpose, a set of equations to handle the numerical computation of the two-dimensional flow field and the evolution of the bed and surface texture (Exner equation and the so-called Hirano model) is introduced. Since the resulting system of equations is not fully hyperbolic, the bed and sorting celerities may not be directly computed from the characteristics theory. However, numerical estimations for the wave celerities are provided and to ensure conservation of the system and to automatically control the numerical stability of the explicit scheme used to solve the system of equations. Additionally, the formulation presented herein does not impose any constraint on the magnitude of the gradients (in the flow field, bed topography and surface texture). Our formulation solves, in a self-stable way, the two-dimensional morphodynamics using the active layer model in its full extension, i.e. assuming that the time-varying surface texture affects both the thickness of the active layer and the bed roughness.

The work is outlined as follows: Section 2 describes the mathematical model while in Section 3 the numerical strategy is explained. Section 4 presents the numerical results obtained, validated with a set of one and two-dimensional test cases and with a two-dimensional experimental test subjected to rapid variations of both flow and channel features. In Section 5 conclusions arising from the work are described.

2. Mathematical model

The mathematical model presented for modelling river morphodynamic is based on the coupled system of equations formed by the 2D shallow water equations to describe the hydrodynamics and the 2D Exner equation, extended to multiple grain sizes, to describe the morphological evolution of the river bed (elevation and surface grain size distribution or texture).

2.1. Hydrodynamic model

Hydrodynamic is formulated by means of the depth averaged shallow water equations. Mass and momentum conservation form a system of equations, which, in 2D Cartesian coordinates, can be written as follows

$$\frac{\partial \mathbf{U}}{\partial t} + \frac{\partial \mathbf{F}(\mathbf{U})}{\partial x} + \frac{\partial \mathbf{G}(\mathbf{U})}{\partial y} = \mathbf{S}_\tau + \mathbf{S}_b \tag{1}$$

where

$$\mathbf{U} = (h, hu, hv)^T \tag{2}$$

are the conserved flow variables with h representing water depth and (u, v) the depth averaged components of the velocity vector in the longitudinal x and transversal y coordinates, respectively. The hydrodynamic fluxes $\mathbf{F}$ and $\mathbf{G}$ in (1) are given by

$$\begin{aligned} \mathbf{F} &= \left(hu, hu^2 + \frac{1}{2} g h^2, huv \right)^T \\ \mathbf{G} &= \left(hv, huv, hv^2 + \frac{1}{2} g h^2 \right)^T \end{aligned} \tag{3}$$

The term $\mathbf{S}_\tau$ in (1) accounts for the frictional effects on the bed as

$$\mathbf{S}_\tau = \left(0, -\frac{\tau_{b,x}}{\rho}, -\frac{\tau_{b,y}}{\rho} \right)^T \tag{4}$$

where $\tau_{b,x}, \tau_{b,y}$ are the bed shear stresses in the x and y direction respectively and ρ is the density of the water. Shear stresses have been evaluated by means of the Manning's law which in 2D is written as follows

$$\begin{aligned}\tau_{b,x} &= gh\frac{n^2u\sqrt{u^2+v^2}}{h^{1/3}} \\ \tau_{b,y} &= gh\frac{n^2v\sqrt{u^2+v^2}}{h^{1/3}}\end{aligned} \tag{5}$$

where n is the roughness Manning's coefficient which has to be evaluated taking into account the surface texture as it is described in further subsection. Finally, the term $\mathbf{S}_b$ in (1) accounts for the the pressure force along Cartesian coordinates x and y respectively.

$$\mathbf{S}_b = (0,\ ghS_{ox}, ghS_{oy})^T \tag{6}$$

where $S_{ox} = \partial z/\partial x$ and $S_{oy} = \partial z/\partial y$ are the bed slope in the x and y direction.

2.2. Bed and surface texture evolution model. Hirano's active layer model

The evolution of bedload-dominated channels has been traditionally modelled by using the classical Exner equation for conservation of mass of sediment [2]. This equation, however, does not account for the evolution of the surface grain size distribution. Thus, when the bed surface is composed of mixtures of grain sizes, particle interactions need to be conservatively accounted for in the mathematical model. Temporal and spatial changes in the surface grain size distribution can be reproduced by means of the active layer and the sediment conservation equations introduced by Hirano [24, 46]. The mathematical model proposed by [24] is extended to two-dimensional domains.
Exner equation for the conservation of mass of sediment states that the rate of change of bed elevation within a control volume is driven by the sediment fluxes crossing the boundaries of that volume. In 2D, such equation is written as follows

$$\frac{\partial \eta}{\partial t} + \xi\frac{\partial q_{b,x}}{\partial x} + \xi\frac{\partial q_{b,y}}{\partial y} = 0 \tag{7}$$

where η is the bed elevation, $\xi = \frac{1}{1-p_b}$, p_b is the porosity of the sediment mixture, $q_{b,x}$ and $q_{b,y}$ denote volumetric sediment transport rates per unit width along the Cartesian coordinates.
Following the methodology proposed by [24], the Exner equation is then extended to sediment mixtures assuming that (i) the grain size distribution

of the bed surface is divided in N discrete fractions, (ii) F_s are the frequencies of each grain size on the surface (subscript s denotes the particle class and ranges from 1 to N) and (iii) that a constant density is assumed for all sizes, given that all sediment on the channel bed has originated from a common source. Each sediment fraction is associated with a characteristic grain diameter, D_s.

Each particle size may be transported at different rates. Let us denote q_{bs} the fractional sediment transport rate associated to grain size s, which is obtained as the product of the sediment transport capacity that the flow is able to mobilize, q^0_{bs} and the proportion of sediment of that particular grain size on the bed surface F_s. q^0_{bs} is computed through a closure equation as shown below. Hence, the sediment fluxes are written in terms of both flow and bed characteristics as,

$$q_{bs} = F_s q^0_{bs} \tag{8}$$

This surface-based formulation[26] assures that, regardless of the magnitude of the the fractional sediment transport capacity q^0_{bs}, $q_{bs} = 0$ if the fraction s is not present on the bed. Finally, the total sediment transport rate, q_b is obtained as the sum of the sediment fluxes of each grain size s,

$$q_b = \sum_{s=1}^{N} q_{bs} \tag{9}$$

Bedload and surface textures vary in time, adjusting to changes in the flow field and bed topography. [46] and more recently [44] conceptualize the channel bed to be formed by two layers which are defined in Figure 1:(i) an uppermost active, exchange or surface layer, the thickness of which, L_a, extends from the bed surface downwards and (ii) a substrate layer, placed underneath the active layer.

The active layer accounts for the average uppermost bed layer that contributes to sediment transport. Therefore, all particles entrained into bedload are supplied from the active layer. Under these conditions, the probability of a particle to be entrained per unit time is constant and equal to 1, [25]. This implies that the probability for substrate particles to be entrainment is zero. Thus, substrate texture does not affect sediment transport rates and their texture. The vertical discrete fraction distribution of each s grain size in the bed f_s, presents a discontinuity depending on the vertical position, z

$$f_s = \begin{cases} F_s(x,y,z,t) & if \quad \eta - L_a < z < \eta \\ f_{ss}(x,y,z) & if \quad z < \eta - L_a \end{cases} \tag{10}$$

where f_{ss} are the fractions of the substrate which do not vary in time but may vary in the longitudinal and transverse directions, i.e. x and y Cartesian coordinates. Of particular interest is the variation of f_{ss} along the vertical coordinate which represents the stratigraphy of the bed at any given point. The non-time dependency of f_{ss} is true when the river bed at a particular location undergoes a single phase of aggradation or degradation. Multiple stages of bed aggradation/degradation change the stratigraphy of the bed over time. For the sake of simplicity, the present formulation does not account for such temporal changes. Additionally, bedload transport rates associated with each grain size, which are allowed to evolve over time, are denoted as $f_{bs} = q_{bs}/q_b$.

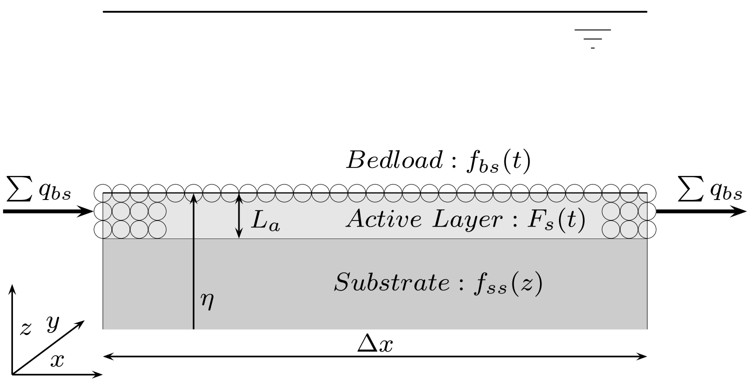

Figure 1: Two bed layer model

All sediment fractions described above must be conserved. Therefore the following constraints must be fulfilled

$$\sum_{s=1}^{N} F_s = 1 \qquad \sum_{s=1}^{N} f_{bs} = 1 \qquad \sum_{s=1}^{N} f_{ss} = 1 \tag{11}$$

The equation for the conservation of mass of each discrete grain size fraction V_s present on the bed is derived next. The application of the Reynolds transport theorem and the mass balance equation on an arbitrary control volume Ω yields the general integral equation for the conservation of sediment for the s-th particle size

$$\frac{\mathrm{d}V_s}{\mathrm{d}t} = \frac{\mathrm{d}}{\mathrm{d}t}\int_{\Omega} \rho(x,t) d\Omega = 0 \Leftrightarrow \frac{\partial}{\partial t}\int_{\Omega} \rho d\Omega + \oint_{\Gamma} \rho \mathbf{u_r} \mathbf{n} d\Gamma = 0 \qquad (12)$$

where V_s is the fractional mass of sediment within the control volume Ω, Γ represents mobile and fixed boundaries of the control volume the mass fluxes flow across, $\mathbf{u_r}$ is the relative velocity between the flow velocity and the speed at which the boundary Γ moves, and $\mathbf{n}$ is the outward unit vector normal to Γ.

The time evolution of V_s in equation (12) is computed taking into account the fractional mass of sediment within the control volume ,represented by the first volume integral in the right hand-side equation (12), and the sediment fluxes through the boundaries of the domain, accounted by the second contour integral in equation (12). The fractional mass is evaluated as

$$V_s = \int_{\Omega} \rho d\Omega = \int_0^{\eta} \int_{A(x,y)} \rho_s f_s \left(1 - p_b\right) dA dz \qquad (13)$$

where $A(x, y)$ is the area across which sediment moves vertically. For this case $A(x, y) = \Delta x \Delta y$. ρ_s is the density of the sediment. Then, equation (13) becomes

$$V_s = \int_0^{\eta} \rho_s f_s \left(1 - p_b\right) \Delta y \Delta x dz \qquad (14)$$

The integral in (14) is split in two parts to account for the vertical discontinuity of the bed stratigraphy f_s in (10), which has been sketched in Figure 1

$$V_s = \rho_s \left(1 - p_b\right) \Delta y \Delta x \left[\underbrace{\int_0^{\eta - L_a} f_{ss} dz}_{\textit{Substrate}} + \underbrace{\int_{\eta - L_a}^{\eta} F_s dz}_{\textit{Active Layer}} \right] \qquad (15)$$

As stated earlier in (10) the substrate fraction f_{ss} may depend on the vertical coordinate z on stratified beds. The second integral in (15) involving the active layer texture F_s represents the fractional volume of sediment within this layer. As stated above, F_s is assumed to be constant within the active layer, L_a. Bearing these hypotheses in mind, the rate of change of the volume of sediment V_s in (15) is

$$\frac{\partial V_s}{\partial t} = \rho_s (1 - p_b) \Delta y \Delta x \frac{\partial}{\partial t} \left[\int_0^{\eta - L_a} f_{ss} dz + F_i L_a \right] \tag{16}$$

The temporal evolution of the mass of sediment V_s, i.e. the integral in the right hand-side of (16) can be rewritten by applying the Leibnitz' rule

$$\frac{\partial V_s}{\partial t} = \rho_s (1 - p_p) \Delta y \Delta x \left[f_{ss(z=\eta - L_a)} \frac{\partial}{\partial t} (\eta - L_a) + \frac{\partial}{\partial t} F_s L_a \right] \tag{17}$$

The term $f_{ss(z=\eta-L_a)}$ represents the fractional exchange of material between the active layer and the substrate, hereafter denoted f_{es}. This term depends on whether bed aggrades or degrades [30, 47]

$$f_{es} = \begin{cases} f_{ss} & if \;\; \frac{\partial \eta}{\partial t} < 0 \\ \alpha F_s + (1 - \alpha) f_{bs} & if \;\; \frac{\partial \eta}{\partial t} > 0 \end{cases} \tag{18}$$

where α is a parameter ranging between 0 and 1 and that needs to be calibrated. Substrate fractions are considered if degradation occurs. Conversely, a linear combination of the surface and bedload transport textures is taken in case of aggradation.

The net flux of sediment across the boundaries of the control domain (contour volume in the right hand-side of (12)) is denoted as Ψ_s and it is computed as

$$\Psi_s = \oint_\Gamma \rho \mathbf{u_r} \mathbf{n} d\Gamma = \rho_s \Delta y \left(q_{bs,x+\Delta x} - q_{bs,x} \right) + \rho_s \Delta x \left(q_{bs,y+\Delta y} - q_{bs,y} \right) \tag{19}$$

Finally, gathering equation (17) and (19), the sediment mass balance for the fraction s in (12) can be expressed as

$$(1 - p_b) \left[f_{es} \frac{\partial}{\partial t} (\eta - L_a) + \frac{\partial}{\partial t} (F_s L_a) \right] = -\frac{\partial q_{bs,x}}{\partial x} - \frac{\partial q_{bs,y}}{\partial y} \tag{20}$$

If the bed is composed of uniform material, fractions f_{es} and F_s are constant in time and equal to 1. Substituting these values in (20) yields the classical Exner equation for uniform grain sizes [44].

2.2.1. Weak-hyperbolicity strategy

The way by which equation (20) is solved is the original contribution of this work. A detailed description of the proposed method is outlined below.

F_sL_a is the conserved variable in (20). This term expresses the fractional volume of sediment within the active layer. The time variation of this variable is balanced by Ψ_s^v and Ψ_s^h (Figure 2). Rearranging terms, equation (20) can be rewritten as

$$\frac{\partial}{\partial t}(F_sL_a) = \underbrace{-\frac{1}{1-p_b}\left(\frac{\partial q_{bs,x}}{\partial x} + \frac{\partial q_{bs,y}}{\partial y}\right)}_{\Psi_s^v} \underbrace{- f_{es}\frac{\partial}{\partial t}(\eta - L_a)}_{\Psi_s^h} \tag{21}$$

Mathematical advantages arise from expressing the rate of change of the surface fractions as in (21). Namely, although (21) is not a hyperbolic equation, a wave speed at which perturbation of the surface texture propagates λ_{F_s} can be estimated through the sediment fluxes as follows,

$$\frac{\partial}{\partial t}(F_sL_a) + \xi\left(\frac{\partial q_{bs,x}}{\partial x} + \frac{\partial q_{bs,y}}{\partial y}\right) = -f_{es}\frac{\partial}{\partial t}(\eta - L_a) \tag{22}$$

$$\lambda_{F_s} \approx \xi\frac{\partial \mathbf{q_{bs}}}{\partial F_sL_a} = \xi\frac{\partial \mathbf{q_{bs}}^0 F_s}{\partial (F_sL_a)} \tag{23}$$

where $\mathbf{q}_{bs}^0 = \left(q_{bs,x}^0, q_{bs,y}^0\right)$, being $q_{bs,x}^0$ the sediment discharge in the longitudinal direction and $q_{bs,y}^0$ the sediment discharge in the transversal direction. This wave speed was first estimated for uniform material in [14]. Here, this idea has been extended to heterogeneous sediment. The wave speed provides information of the celerity at which the surface texture changes, hereafter referred to as sorting celerity. This sorting celerity needs to be retained to ensure numerical stability of the solver, [48, 14], and also for the upwinding technique considered in the next section.

2.2.2. Closure equations

$4+N$ equations need to be solved. 3 equations arise from the hydrodynamic model, i.e. mass and momentum conservation equations, system (1), and the rest $1+N$ equations are derived from the morphodynamic model (the classical Exner and Hirano equations, (7) and (22) to update the bed elevation and the surface fractions respectively). The number of dependent variables is

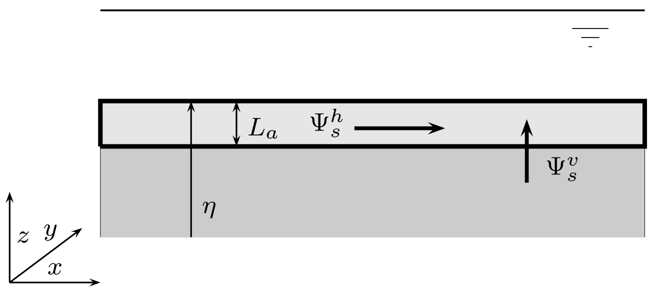

Figure 2: Mass conservation in active layer

thus equal to $4 + N$: (i) the flow depth h, (ii) the depth-averaged velocities in Cartesian coordinates u and v, (iii) the bed elevation η and (iv) the surface fractions on the bed surface F_s.
However, 3 complementary equations are needed to describe the bed roughness (expressed in terms of the Manning's coefficient n in (5)), sediment transport rates q_{bx}, q_{by} in (7) and the thickness of the active layer L_a in (22).

Bed roughness
Bed shear stresses are computed by means of the Manning's equation, which takes the roughness of the bed n into account. This roughness, which is associated with the texture of the bed, is computed by using the Manning-Strickler formula [49]:

$$n = \frac{1}{26} D_{90}^{1/6} \tag{24}$$

where D_{90} is the 90 percentile of the bed, i.e. the grain size of the surface texture such that 90% of the bed is finer. Equation (24) implies that when the bed surface is composed of sediment mixtures, the surface texture (i) may be non-uniform across the domain and (ii) it may vary in time at a given location (10). Therefore, under these conditions, n is not constant. Conversely, it varies according to the temporal and spatial evolution of D_{90}.

Bed load sediment transport capacity formula
The fractional bedload transport capacity q_{bs}^0 can be obtained by using probability laws [50, 2] or by means of empirically fitted expressions to experimental data (e.g. [51, 52, 53]). The modulus of the sediment transport rate, $\mathbf{q}_{bs}^0 = \left(q_{bs,x}^0, q_{bs,y}^0\right)$ is

$$\left|\mathbf{q}_{bs}^{0}\right| = \sqrt{\left(q_{bs,x}^{0}\right)^{2} + \left(q_{bs,y}^{0}\right)^{2}} \quad (25)$$

Bedload transport rates are usually expressed in dimensionless form by the Einstein number

$$\Phi_s = \frac{|\mathbf{q}_{bs}^{0}|}{\sqrt{g(r-1)D_s^3}} \quad (26)$$

where $r = \rho_s/\rho_w$ is the ratio between sediment (ρ_s) and water (ρ) densities. Dimensionless sediment transport rates are usually expressed in terms of the dimensionless shear stress or Shields number as

$$\theta_s = \frac{|\mathbf{T}_b|}{g(\rho_s - \rho_w)D_s} \quad (27)$$

where $\mathbf{T}_b = (\tau_{b,x}, \tau_{b,y})$ is the shear stress at the bed obtained assuming steady flow through the Manning's coefficient. This allows expressing $|\mathbf{T}_b|$ as

$$|\mathbf{T}_b| = \sqrt{\tau_{b,x}^2 + \tau_{b,y}^2} \quad (28)$$

which, with the aid of (5), leads to the following expression for the Shields number:

$$\theta_s = \frac{n^2}{(s-1)D_s h^{1/3}}(u^2 + v^2) = \frac{n^2}{(s-1)D_s h^{1/3}}|\mathbf{u}|^2 \quad (29)$$

Fractional bedload transport rates are calculated using the sediment transport capacity formula derived by [54]. This equation, based on the difference between the acting dimensionless bed shear stress θ_s and the dimensionless critical shear stress for the onset of motion θ_{cs} associated with the sth grain size, is expressed as

$$\Phi_s = 17(\theta_s - \theta_{cs})(\sqrt{\theta_s} - \sqrt{\theta_{cs}}) \quad (30)$$

θ_{cs} associated with the grain size s is obtained by using the hiding/exposure function proposed by [55] as

$$\frac{\theta_{cs}}{\theta_{c50}} = \begin{cases} 0.843\left(\frac{D_s}{D_{50}}\right)^{-1} & \frac{D_s}{D_{50}} \leq 0.4 \\ \left(\frac{log19}{log\left(19\frac{D_s}{D_{50}}\right)}\right)^2 & \frac{D_s}{D_{50}} > 0.4 \end{cases} \quad (31)$$

where θ_{c50} and D_{50} are the dimensionless critical shear stress and grain size associated with the median diameter of surface texture, respectively.

Active layer

The definition of the active layer model requires a closure relation to describe its thickness. A constant value of L_a has been commonly assumed. However, as stated by [41], this approach deeply affects the bed celerity. In one-dimensional numerical models, L_a is usually associated with a characteristic length of the river bed (e.g. some reference sediment diameter in the plane bed case, the dune height in case of the appearance of bedforms). Since the active layer thickness accounts for the fluctuations of the bed elevation, D_{90} is usually taken as the reference grain size to which its thickness is related. Hence, the thickness of the active layer is expressed as

$$L_a = KD_{90} \tag{32}$$

where K, ranges between 1 and 3 [30, 31, 32, 33, 34, 36, 37, 38, 39].

3. Numerical scheme

3.1. Hydrodynamic numerical scheme

The system of equations in (1) is integrated using the Gauss theorem in a grid cell Ω_L. $\mathbf{n}$ denotes the outward vector to the cell edge Ω_L and $\mathbf{E_n} = \mathbf{F}n_x + \mathbf{G}n_y$.

$$\frac{\partial}{\partial t}\int_{\Omega_L} \mathbf{U} d\Omega + \oint_{\partial\Omega_L} \mathbf{E_n} dl = \int_{\Omega_L} (\mathbf{S}_\tau + \mathbf{S}_b) d\Omega \tag{33}$$

The second integral in (33) can be explicitly obtained as a sum over the cell edges,

$$\frac{\partial}{\partial t}\int_{\Omega_L} \mathbf{U} d\Omega + \sum_{k=1}^{NE}\int_{l_k} \mathbf{E}_{\mathbf{n}k} dl_k = \int_{\Omega_L} (\mathbf{S}_\tau + \mathbf{S}_b) d\Omega \tag{34}$$

where dl_k is the length of each edge of a cell and NE is the number of edges of a grid cell Ω_L. The values of the conserved variables inside the cells, $\mathbf{U}_L^n$, are assumed piecewise constant, i.e. averaged within each cell A_L. Thus, an uniform value at each cell A_L is obtained

$$\mathbf{U}_L^n = \frac{1}{A_L}\int_{\Omega_L} \mathbf{U}(x,y,t^n)d\Omega \tag{35}$$

Substituting the piecewise assumption, (35), in (34), this latter equation is written as

$$\frac{\partial}{\partial t}\int_{\Omega_L} \mathbf{U}d\Omega + \sum_{k=1}^{NE}(\mathbf{E_n})_k l_k = \sum_{k=1}^{NE}\mathbf{S}_{\tau\mathbf{n}} l_k + \sum_{k=1}^{NE}\mathbf{S}_{b\mathbf{n}} l_k \tag{36}$$

where l_k is the length of each edge of a cell and $\mathbf{S}_{b\mathbf{n}}$ and $\mathbf{S}_{\tau\mathbf{n}}$ are the integrals of the friction and bed slope terms [9].
The numerical scheme to solve (36) is constructed by means of an approximate Jacobian matrix $\widetilde{\mathbf{J}}_{\mathbf{n},k}$ at each edge k between neighbouring cells and defined through the normal fluxes between these adjacent cells $\mathbf{E_n}$

$$(\delta\mathbf{E_n})_k = \widetilde{\mathbf{J}}_{\mathbf{n},k}\delta\mathbf{U}_k \tag{37}$$

where $\delta(\mathbf{E_n})_k = (\mathbf{E}_R - \mathbf{E}_L)_{\mathbf{n}_k}$, $\delta\mathbf{U}_k = \mathbf{U}_R - \mathbf{U}_L$, and $\mathbf{U}_L$ and $\mathbf{U}_R$ are the initial values of the conserved variables at adjacent cells L and R.
From this approximate Jacobian matrix a set of three real eigenvalues $\widetilde{\lambda}_k^m$ and eigenvectors $\widetilde{\mathbf{e}}_k^m$ are obtained. From this definition, it is possible to define two approximate matrices $\widetilde{\mathbf{P}} = (\widetilde{\mathbf{e}}^1, \widetilde{\mathbf{e}}^2, \widetilde{\mathbf{e}}^3)$ and $\widetilde{\mathbf{P}}^{-1}$ which allow to diagonalize the Jacobian matrix,

$$\widetilde{\mathbf{J}}_{\mathbf{n},k} = \widetilde{\mathbf{P}}_k\widetilde{\mathbf{\Lambda}}_k\widetilde{\mathbf{P}}_k^{-1} \tag{38}$$

being $\widetilde{\mathbf{\Lambda}}_k$ the matrix which contains the eigenvalues in the diagonal. In addition, the vector of conserved variables, $\mathbf{U}$ is then split through the matrix of eigenvectors, $\widetilde{\mathbf{P}}$, as

$$\delta\mathbf{U}_k = \widetilde{\mathbf{P}}_k\widetilde{\mathbf{A}}_k = \sum_{m=1}^{3}(\widetilde{\alpha}\widetilde{\mathbf{e}})_k^m \tag{39}$$

The source terms in (36) are also projected onto the matrix of eigenvectors, $\widetilde{\mathbf{P}}$ to guarantee the exact equilibrium between fluxes and source terms,

$$(\mathbf{S}_{b\mathbf{n}}, \mathbf{S}_{\tau\mathbf{n}})_k = \widetilde{\mathbf{P}}_k\widetilde{\mathbf{B}}_k = \sum_{m=1}^{3}\left(\widetilde{\beta}\widetilde{\mathbf{e}}\right)_k^m \tag{40}$$

Based on the above information the volume integral in the cell at time t^{n+1} is expressed as

$$\mathbf{U}_L^{n+1} = \mathbf{U}_L^n - \sum_{k=1}^{NE} \sum_{m=1}^{3} (\widetilde{\lambda}^- \widetilde{\alpha} - \widetilde{\beta}^-)_k^m \widetilde{\mathbf{e}}_k^m l_k \frac{\Delta t}{A_L} \tag{41}$$

The superscript minus in (41) implies that only the incoming waves are considered for updating the values of each cell, defining $\lambda^- = \frac{1}{2}(\lambda - |\lambda|)$. Splitting the fluxes as shown in equations (39)-(40) allows no special treatment at the boundary cells: the conserved variables $\mathbf{U}$ are updated in time by means of the incoming information which is averaged at each edge. Complete details can be found in [9]

To avoid numerical instabilities, time step Δt has to reduced sufficiently so that there are no interactions of waves between neighbouring cells. The Courant dimensionless number, CFL is used to control the stability of the numerical scheme

$$CFL = \frac{\Delta t^{hydro}}{\Delta t^{\widetilde{\lambda}}} \quad \text{where} \quad \Delta t^{\widetilde{\lambda}} = \frac{\min(\chi_L, \chi_R)}{\max |\widetilde{\lambda}^m|} \tag{42}$$

where the superscript m ranges from 1 to 3, according to the three equations (1) for the hydrodynamic part. χ is the relevant distance for numerical stability which, in a two-dimensional model, must consider the area of the adjacent cells L and R and the length of the shared k edges l_k[56],

$$\chi_L = \frac{A_L}{\max_{k=1,NE} l_k} \tag{43}$$

Equation (42) allows choosing an appropriate Δt such that it always falls within the stability region as

$$\Delta t^{hydro} \leq CFL\ \Delta t^{\widetilde{\lambda}} \tag{44}$$

with CFL=1 in the case of 1D configurations and CFL≤1/2 in the case of triangular unstructured grids.

3.2. Morphodynamic numerical scheme

3.2.1. Bed elevation updating

Following [14], sediment conservation equation (7) needs to be integrated in a grid cell Ω_L

$$\frac{\partial}{\partial t}\int_{\Omega_L}\eta d\Omega + \oint_{\Gamma}\xi(\mathbf{q_{bn}})d\Gamma = 0 \tag{45}$$

where it is worth recalling that $\mathbf{q}_{bn} = (q_{b,x}n_x + q_{b,y}n_y)$ and also $q_{b,x} = \sum_{s=1}^{N} q_{bs,x}$, $q_{b,y} = \sum_{s=1}^{N} q_{bs,y}$ where N is the number of sediment grain sizes contained in the mixture.
Using Gauss theorem, assuming a piecewise representation of the variable η and noting that the second integral can be expressed as the sum of fluxes across the edges of the cell Ω_L,

$$\frac{\partial}{\partial t}\int_{\Omega_L}\eta d\Omega + \sum_{k=1}^{NE}\xi\int \mathbf{q_{bn}}_k dl_k = 0 \tag{46}$$

Then, the Godunov first order method is built through a flux scheme, considering outcoming and incoming fluxes through the edges of the cell. Hence the bed elevation η is updated as

$$\eta_L^{n+1} = \eta_L^n - \sum_{k=1}^{NE}\xi q^*_{bn,k}\frac{\Delta t\ l_k}{A_L} \tag{47}$$

where total sediment fluxes across each edge are written as the sum of the fractional bedload transport rate s,

$$q^*_{bn,k} = \sum_{s=1}^{N} q^*_{bsn,k} \tag{48}$$

The fractional bedload transport rates $q^*_{bsn,k}$ are computed following the upwind philosophy, i.e., taking the values from left or right side according the sign of the celerity,

$$q^*_{bsn,k} = \begin{cases} q_{bsn,L} & \text{if} \quad \widetilde{\lambda}_{\mathbf{bsn},k} > 0 \quad with \quad q_{bsn,L} = (q_{bs,x}n_x + q_{bs,y}n_y)_L \\ q_{bsn,R} & \text{if} \quad \widetilde{\lambda}_{\mathbf{bsn},k} < 0 \quad with \quad q_{bsn,R} = (q_{bs,x}n_x + q_{bs,y}n_y)_R \end{cases} \tag{49}$$

being $q_{bsn,L}$ and $q_{bsn,R}$ the bedload transport rates associated with the s grain size across neighbouring cells (L, R). $\widetilde{\lambda}_{\mathbf{bsn},k}$ is the numerical bed celerity, i.e. the speed at which changes in the bed propagate along the domain, estimated as

$$\widetilde{\lambda}_{\mathbf{bsn},k} \approx \frac{\delta(\xi q_{bsn,k})}{\delta\eta} \tag{50}$$

where $\delta q_{bsn,k} = \left(q^0_{bsn,R} F_{s,R} - q^0_{bsn,L} F_{s,L}\right)$ is the normal sediment transport flux across the k edge and $F_{s,R}$ and $F_{s,L}$ are the content of the grain size s on the bed surface in cells R and L respectively.

At this stage, the stability criterion has to be revisited to include the estimations of bed celerities defined in (50). Hence, the time step limitation for the bedload transport is imposed as

$$\Delta t^{bed} = CFL \Delta t^{\widetilde{\lambda_b}} \quad \text{where} \quad \Delta t^{\widetilde{\lambda_b}} = \frac{\min(\chi_L, \chi_R)}{|\widetilde{\lambda}_{\mathbf{bsn},k}|} \tag{51}$$

with CFL=1 in the case of 1D configurations and CFL≤1/2 in the case of triangular unstructured grids.

Considering both time restrictions, hydrodynamic and morphodynamic wave speeds, the following stability criterion is defined so that numerical stability is numerically ensured

$$\Delta t = \min\left(\Delta t^{bed}, \Delta t^{hydro}\right) \tag{52}$$

A detailed description of both hydrodynamic and morphodynamic numerical schemes can be found in [14].

3.2.2. Surface grain size fraction update

The following physically-based, self-stable numerical scheme is introduced. We start this mathematical development from (21)

$$\frac{\partial}{\partial t}(F_s L_a) = -\frac{1}{1-p_b}\left(\frac{\partial q_{bs,x}}{\partial x} + \frac{\partial q_{bs,y}}{\partial y}\right) - f_{es}\frac{\partial}{\partial t}(\eta - L_a) \tag{53}$$

Equation (21) is integrated following the same steps used above: (i) integration over a grid cell Ω_L, (ii) applying the Gauss theorem and (iii) assuming a piecewise representation of the conserved variables. Thus, the Godunov first order method is built through a flux scheme. Therefore, the surface fraction s at cell L is updated as follows,

$$(F_{s_L} L_a)^{n+1} = (F_{s_L} L_a)^n + \Delta t \left[\sum_{k=1}^{NE} \xi \left(-q^*_{bsn,k}\right) \frac{l_k}{A_L} - f_{es_L} \frac{\Delta(\eta - L_a)}{\Delta t}\right] \tag{54}$$

where the last term associated with $(\eta - L_a)$ is computed for simplicity implicitly, i. e. evaluating that term as a source term using known quantities from the present and past time levels [57, 33, 34, 38] . Additionally, the flux associated with the fractional transport rate $q^*_{bsn,k}$ between the cells L and R is evaluated following an upwind technique as follows,

$$q^*_{bsn,k} = \begin{cases} q_{bsn,L} & \text{if} \quad \widetilde{\lambda}_{F_{s,k}} > 0 \quad with \quad q_{bsn,L} = \left(q_{bs,x} n_x + q_{bs,y} n_y\right)_L \\ q_{bsn,R} & \text{if} \quad \widetilde{\lambda}_{F_{s,k}} < 0 \quad with \quad q_{bsn,R} = \left(q_{bs,x} n_x + q_{bs,y} n_y\right)_R \end{cases} \tag{55}$$

where the sorting celerities $\widetilde{\lambda}_{F_{s,k}}$ are defined as

$$\widetilde{\lambda}_{F_{s,k}} \approx \frac{\delta(\xi q_{bsn,k})}{\delta\left(F_s L_a\right)} \tag{56}$$

where $\delta q_{bsn,k} = \left(q^0_{bsn,R} F_{s,R} - q^0_{bsn,L} F_{s,L}\right)$ is the normal flux of the sediment transport rate across the edge k and $\delta F_s L_a = (F_{s,R} L_{a,R} - F_{s,L} L_{a,L})$. Additionally, since mass conservation must be satisfied, the following condition

$$\sum_{s=1}^{N} (F_s L_a) = L_a \tag{57}$$

must be fulfilled. $\widetilde{\lambda}_{F_{s,k}}$ in equation (56) estimates a numerical sorting celerity for each grain size. Therefore, the numerical stability criterion defined by (51) and (52) must include this wave speed. Consequently, the time step restriction for the sorting wave is fixed as

$$\Delta t^{fraction} = CFL \Delta t^{\widetilde{\lambda_{F_s}}} \quad \text{where} \quad \Delta t^{\widetilde{\lambda_{F_s}}} = \frac{\min(\chi_L, \chi_R)}{|\widetilde{\lambda}_{F_s}|} \tag{58}$$

With this new constraint, the time step that governs the stability of the numerical scheme proposed to solve the system of equations formed by (1), (7) and (21) is obtained as

$$\Delta t = \min\left(\Delta t^{fraction}, \Delta t^{bed}, \Delta t^{hydro}\right) \tag{59}$$

This new stability criterion prevents instabilities of the numerical scheme. The performance of the numerical outcomes are presented in the next section.

4. Examples of application: test cases

The weak hyperbolicity strategy outlined in the previous section is now applied to several test cases. The first two test cases aim to analyze the ability of the numerical model to reach equilibrium conditions under aggradational and degradational scenarios. The results of these numerical experiments are compared to a widely used and well established one-dimensional model [39]. The propagation of the surface sediment sorting along the domain is analyzed. The third test case is focused on a two dimensional dam break. The last numerical run presents the comparison of a set of experiments on dam removal with the presence of mixtures. The sediment transport capacity formula proposed by Ashida-Michiue [54] has been used in all simulations. The thickness of the active layer is computed as one time the D_{90}, i.e. $K = 1$, equation (32).

4.1. One dimensional synthetic tests

In a feed experiment in a flume, i.e. when both water discharge and sediment feed rate are introduced in the channel at constant rates, bed slope and surface grain size distribution gradually adjusts to a steady state in which bedload transport rate and its texture at every single point of the channel match those of the feed [58]. Under these conditions, the ability of the numerical scheme to reach a steady state can be easily evaluated. Equation (18) states that the bed response imposes different vertical fluxes of sediment depending on whether the bed aggrades or degrades. Therefore, in order to examine the performance of the numerical model under all possible conditions, two general aggradation and degradation test cases are analyzed.

First, we need to determine the equilibrium conditions for a given initial setup. This occurs when the bedload transport rate and texture are such that the bed does not aggrade or degrade. To do so, we need to apply the selected sediment transport capacity formula for the given initial conditions. If the equilibrium feed rate is then modified but its grain size distribution is fixed, a new equilibrium will be achieved after a process of aggradation/degradation. All the test cases considered herein disturb the initial equilibrium condition by arbitrarily increasing/reducing the feed rate by 35% (see sections below). In order to prevent spurious numerical instabilities arising from the jump in the longitudinal distribution of the sediment transport rates between the channel inlet and the cross-sections downstream once the feed is modified, sediment feed rate is introduced by means of an upstream boundary condition function that gradually adjust the initial sediment transport rate to the desired one, i.e. 35% higher or lower than the one at initial conditions. This function takes the form of a sinusoidal function as follows

$$q_b^{inlet}(t) = q_b^{eq} \sin\left(\frac{\pi}{4} \pm \frac{t}{4996.132}\right)\frac{1}{0.707} \tag{60}$$

where q_b^{inlet} is the feed rate (bedload transport at the inlet), q_b^{eq} is the bedload transport at equilibrium. To achieve the $\pm$ 35%, a lag time of 3924 s is defined ($\sim 4996.132 \cdot \pi/4$). Feed rate is constant and equal to q_b^{eq} hereafter.

All simulations are based on a straight rectangular 6 m-long, 1 m-wide channel and a bed slope S_o=0.002 m/m. A steady stage is considered as an initial configuration for all runs. In order to strengthen the accuracy and the quality of the numerical predictions, three different grain size distributions have been considered under constant water discharge for all cases ($Q = 0.2\ m^3/s$). The vertical texture of the bed is considered equal to the surface texture. Conversely, due to the different surface textures used in the tests, feed rate and texture at the inlet slightly vary for each run. Boundary conditions (feed rate and grain size distribution at the inlet and water surface elevation at the outlet) are different for each test. Recall that the bed roughness (and hence the water depth and the sediment transport rates) changes according to the grain size distribution of the surface (24). Water depth at the outlet results from a steady state calculation reached with the same initial configuration (slope and surface texture) but under fixed-bed conditions. This ensures that the initial condition for the mobile bed calculations is uniform and steady. No fixed bed elevation is imposed at the channel outlet. This implies that the bed at this location evolves in time until a new equilibrium is achieved. However, since the water depth at the outlet has been held constant throughout the simulations, this condition is equivalent to that in which the change in the bed is constrained and a fixed water surface elevation at this station is imposed. The mesh size for all tests is Δx=0.10 m.

4.1.1. One-dimensional degrading tests

Test 1. Texture 1: One grain size.

A uniform size distribution with D_s=2.828 mm is considered (Table 1). Initial and boundary conditions for this test case can be found in Table 1.

test case	N	Grain sizes D_s (mm)	Grain size fractions F_s (-)	D_g (mm)	q_b^{eq} (m^2/s)	$q_{b,feed}$ (m^2/s)	$\eta_{w,o}$ (m)
1	1	2.828	1	2.828	$4.7810 \cdot 10^{-5}$	$3.1079 \cdot 10^{-5}$	0.1921
2	2	1.834 2.181	0.5 0.5	2.000	$4.5717 \cdot 10^{-5}$	$2.9716 \cdot 10^{-5}$	0.1894
3	4	1.541 1.830 2.182 2.593	0.25 0.25 0.25 0.25	2.000	$4.7667 \cdot 10^{-5}$	$3.0984 \cdot 10^{-5}$	0.1921

Table 1: Initial and boundary conditions for all one-dimensional test cases: D_s, F_s grain size distribution of the feed and the bed surface, D_g: mean geometric grain size of the feed and the bed surface, q_b^{eq} sediment transport rate in equilibrium with the initial conditions, $q_{b,feed}$: feed rate, $\eta_{w,o}$: water surface elevation at the outlet.

Figure 3a shows evidences that little changes in the bed are observed after approximately $t = 10800\ s$. Figures 3b and c compare the water discharge and sediment transport rates entering and leaving the flume respectively. Figure 3b demonstrates that the model is conservative as far as the mass of water is concerned. As pointed out in Figure 3c, the initial imbalance of sediment causes the bed to degrade until shortly after $t = 10800\ s$ when the mass of sediment going out matches that entering the flume. This means that the new equilibrium conditions have been achieved.

In order to study the convergence of the numerical scheme, different mesh sizes have been considered. The bed elevation at different positions and with several mesh sizes together with the sediment rate at the inlet is plotted in Figure 4. As the number of cells involved in the calculation increases, differences among results provided by the numerical model decrease. The resulting equilibrium slope for each mesh size is listed in Table 2. Bearing in mind that the reference equilibrium slope is 0.00167 m/m, Table 2 illustrates how the convergence approaches 1 (we use a first order numerical scheme) as the cell size of the mesh Δx gets finer.

Mesh size	S_o (m/m)	*Convergence*
Δx = 0.2 m	0.00160117	-
Δx = 0.1 m	0.00165882	0.88632
Δx = 0.05 m	0.00166058	0.95866
Δx = 0.025 m	0.00166872	0.98991
Δx = 0.0125 m	0.00167011	0.99497

Table 2: Degradation case. 1 Fraction. Summary of the final bed slope convergence with different mesh sizes.

Test 2. Texture 2: two grain sizes.

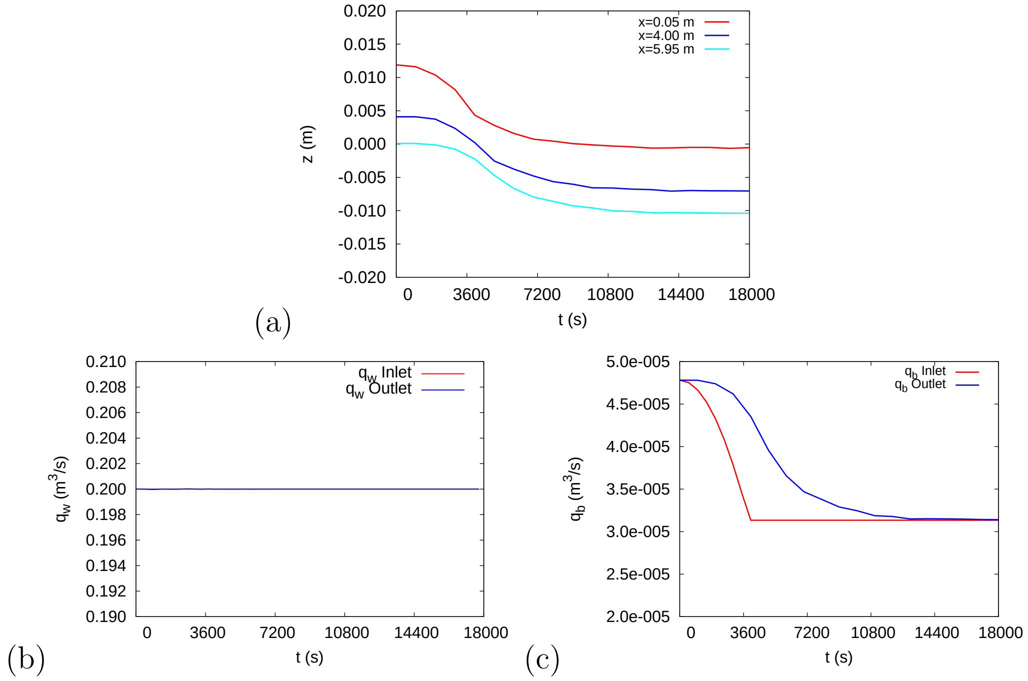

Figure 3: Bed level evolution in time at several points within the channel (a) and water (b) and solid discharge (c) in time. Degradation case. 1 Fraction.

In the second test case, the grain size distribution is composed of two equally distributed grain fractions (Table 1). Initial and boundary conditions for the test are listed in Table 1.

The temporal imbalance in the sediment transport rate at the inlet and the outlet is shown in Figure 5a,b. Figure 5c presents the evolution of the bed elevation at four stations along the channel. The temporal evolution of the two surface fractions at the same four channel stations is illustrated in figures 5d and 5e. These figures show how the fine and the coarse fraction decrease and increase respectively so that the geometric mean size of the bed surface gradually coarsens until approximately $t = 10000\ s$. The small inset panels in Figures 5 illustrate how the surface grain distribution gradually adjust along the channel starting from the uppermost stations. The same trend is suggested in the evolution of the bed elevation in Figure 5c. Figure 5g displays the evolution of the time step associated with each wave speed (hydrodynamic, bed and sorting). Initially, the time step for the numerical simulation is controlled by the sorting celerities. The surface adjustment of the finer

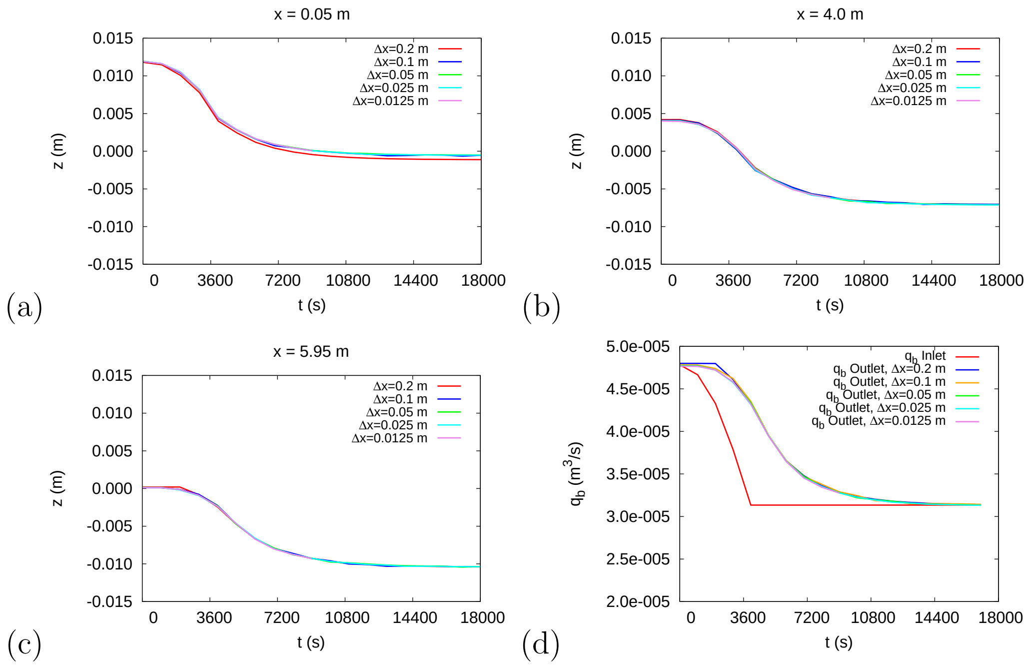

Figure 4: Degradation case. 1 Fraction. Convergence analysis using different mesh sizes.(a)-(c): Temporal evolution of the bed elevation at different channel stations. (d) Temporal evolution of the sediment transport rate at the channel outlet.

fraction is produced much faster than the bed and the hydrodynamic adjustments. This leads to a smaller time steps until the bed gradually adjusts. Note that the time step during the adjustment period of time, $t < 15000s$, is either controlled by the bed or the sorting celerities.

Test 3. Texture 3: Four grain sizes.

This test case consist of a sediment mixture composed of four sediment grain sizes (Table 1).

Figure 6 illustrates similar results to those presented in Figure 5. As expected, the bed surface gradually coarsens (Figure 6d-h) at the same time as the channel degrades -Figure (6c)- in the transient degradational adjustment of the channel. The new steady state is reached between t = 10000 s and t = 15000 s. As with the previous test, time to adjustment increases with the distance downstream. This is noticeable in the bed elevation panel (Figure 6c) but especially in the surface grain size distribution. Further, the adjustment rates of the bed surface (measured by the slope of curves in the small inset panels) gradually decline in the downstream direction.

4.1.2. One-dimensional aggrading tests

The second test case is analogous to the first one but now the new equilibrium profile is attained after a transient aggradational process. To achieve this the initial sediment transport capacity obtained for each grain size using the same initial conditions is increased by 35%. All other variables remain the same as for degradation tests. For the sake of brevity only the results obtained with 2 and 4 fractions are reported (tests 1 and 3 in the previous section and in Table 1).

Figures 7 and 8 illustrate the results of the numerical aggradation experiments when the sediment mixture is composed of two and four grain sizes respectively. These two figures show, from a qualitative point of view, the same results: (i) mass of water is fully conserved right after the commencement of the experiment, (ii) sediment transport rate at the outlet is initially lower than the feed rate and gradually increases until attaining equilibrium conditions at the same time (iii) bed surface coarsens initially in the transient aggradational adjustment of the channel, then it fines as a consequence of the imposed sediment discharge and finally it achieves an equilibrium stage.

Finally, Table 3 compares the computed values obtained with the new numerical model with the reference values obtained with a widely used numerical model [39].

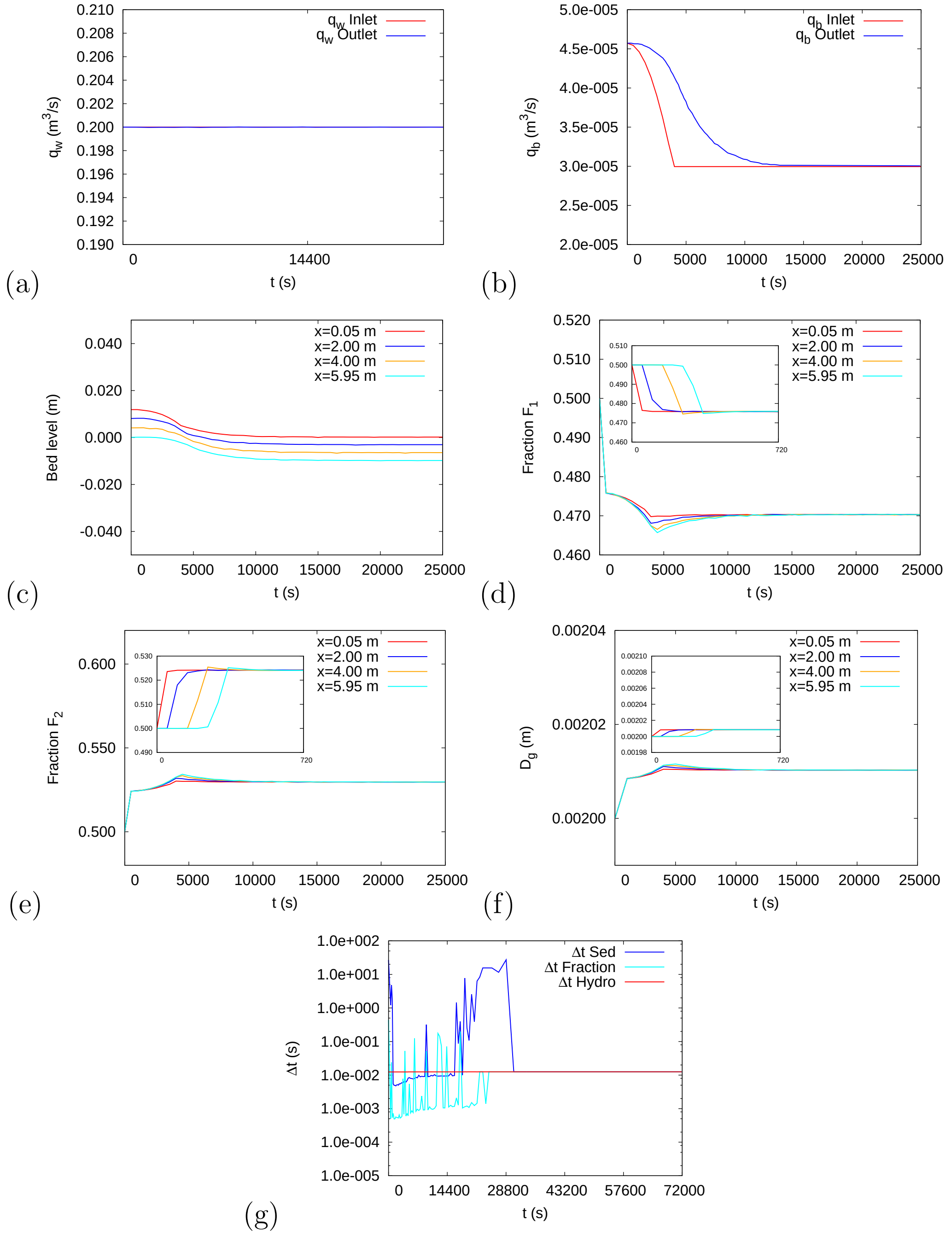

Figure 5: Degradation case. 2 Fractions. Temporal evolution for (a) water discharge, (b) sediment discharge, (c) bed elevation, (d) fraction F_1, (e) fraction F_2, (f) geometric diameter and (g) timestep

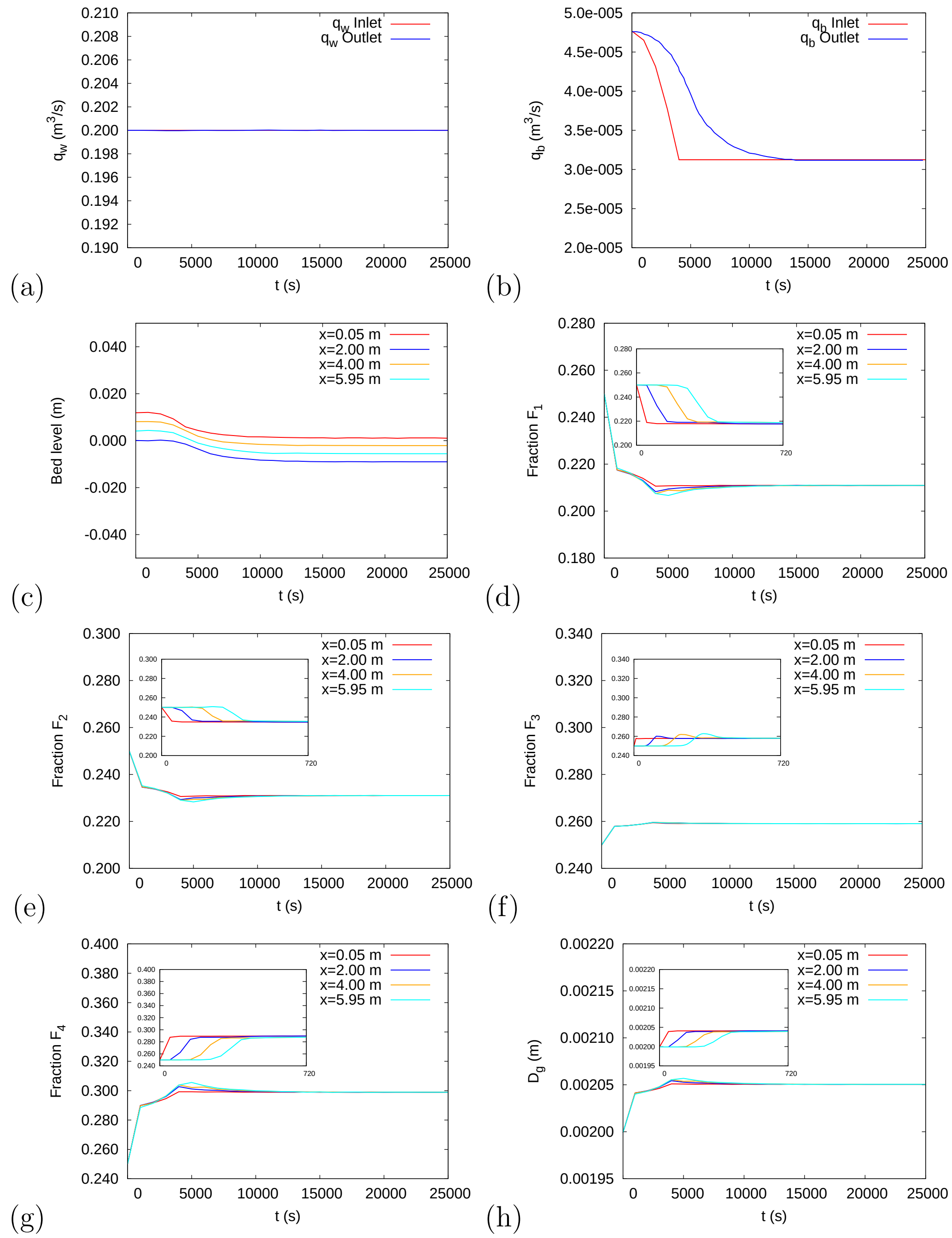

Figure 6: Degradation case. 4 Fractions. Temporal evolution for (a) water discharge, (b) sediment discharge, (c) bed level, (d) fraction F_1, (e) fraction F_2, (f) fraction F_3, (g) fraction F_1 and (h) geometric diameter.

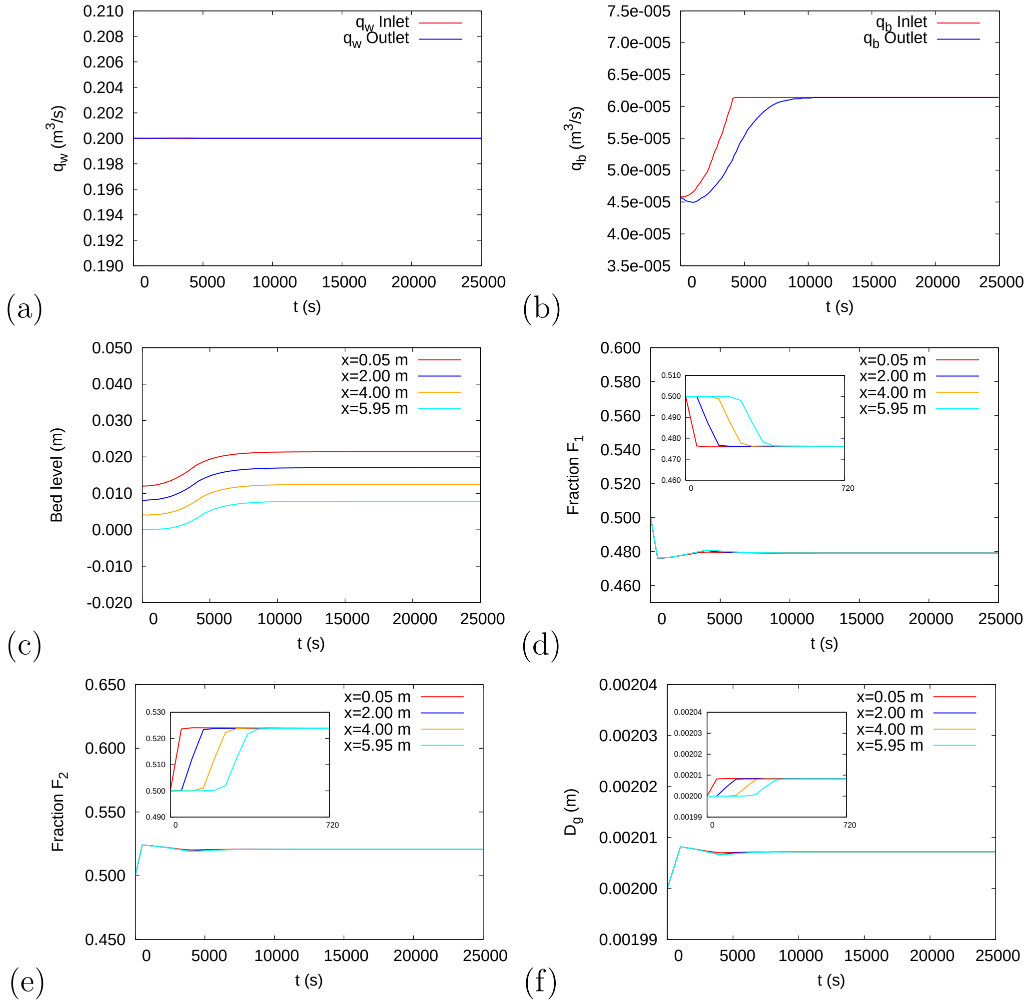

Figure 7: Aggradation case. 2 Fractions. Temporal evolution for (a) water discharge, (b) sediment discharge, (c) bed level, (d) fraction F_1, (e) fraction F_2 and (f) geometric diameter.

Degradation	$S_{o,eq}^{Reference}(m/m)$	$S_{o,eq}^{computed}(m/m)$	$D_{g,eq}^{Reference}(m)$	$D_{g,eq}^{computed}(m)$
1 Fraction	0.001670	0.001658	0.002001	0.001999
2 Fractions	0.001667	0.001663	0.002030	0.002010
4 Fractions	0.001670	0.001697	0.002050	0.002012
Aggradation				
2 Fractions	0.002300	0.002650	0.002007	0.002007
4 Fractions	0.002290	0.002300	0.002035	0.002035

Table 3: Degrading and aggrading test cases. Comparison between the reference and computed values.

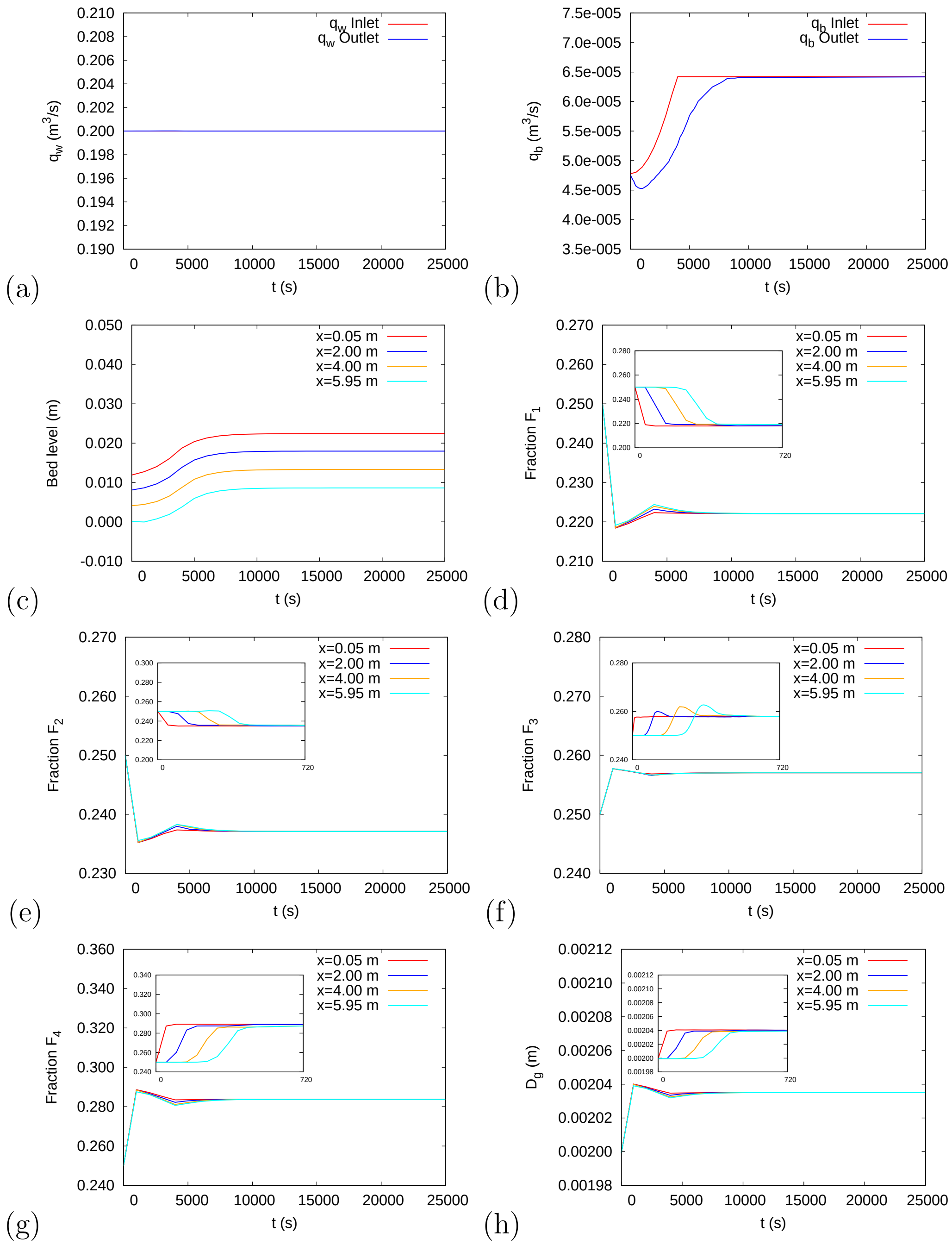

Figure 8: Aggradation case. 4 Fractions. Temporal evolution for (a) water discharge, (b) sediment discharge, (c) bed level, (d) fraction F_1, (e) fraction F_2, (f) fraction F_3, (g) fraction F_4 and (h) geometric diameter.

4.2. Two-dimensional asymmetric dam break

This numerical experiment has been considered for testing the performance of the numerical model under more realistic scenarios where important gradients of the computed variables (bed elevation, flow field and grain size distribution) are observed. This test case consists of an asymmetrical dam break over a dry and erodible bed (Figure 9). The asymmetry arises from the sudden expansion on the left bank of the channel which causes a local erosion around the corner and consequently, sediment deposition downwards. This test is used to examine the behaviour of the numerical model under a highly rapid flow in a two-dimensional geometry. The initial water depth condition has been set 0.25 m upstream the gate, which is located in the middle (Figure 9). An unstructured mesh with a cell size of $0.01m^2$ has been considered and the CFL has been imposed equal to 0.5.

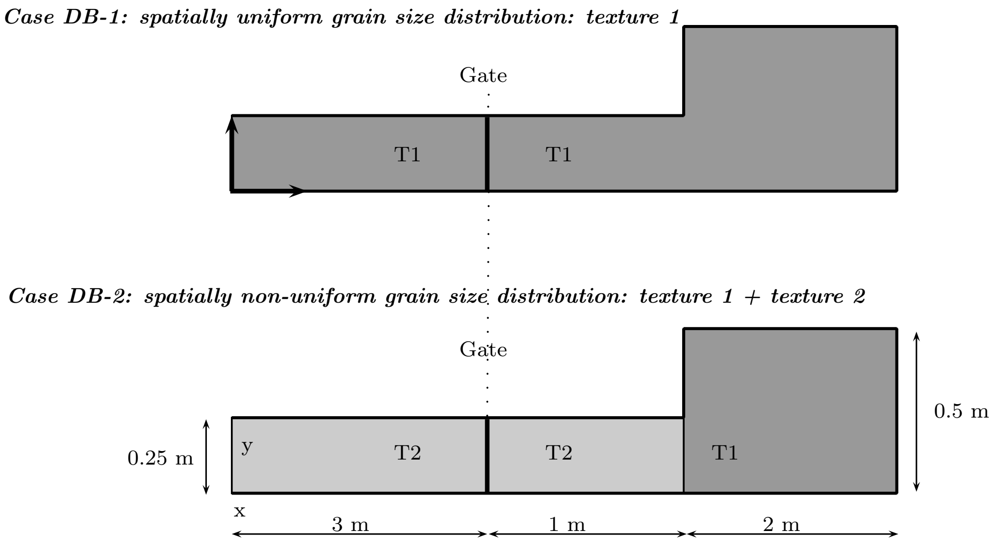

Figure 9: Sketch of the two-dimensional asymmetric dam break: plan view of the spatially uniform grain size distribution Case DB-1 (top) and of the spatially non-uniform grain size distribution Case DB-2 (bottom). T1 and T2 represent the two initial surface textures used in the numerical simulations (Table 4).

Two distinct cases have been considered (Figure 9). In the first case, hereafter referred to as Case DB-1, a grain size distribution formed by four grain classes T1 ($D_g = 5.837\ mm$) constitutes the initial surface texture throughout the domain. The second case, called Case DB-2, considers two different regions as far as the initial surface texture is concerned: the surface texture on the 4 m-long channel (both upstream and downstream of the dam, Figure 9) consists of a mixture T2 formed by four grain classes with $D_g = 1.884$ mm; the surface texture in region 2, which encompasses the last 2 m of the domain, i.e. the expansion of the channel, is composed by the previous grain size distribution T1. Neither water discharge nor feed rate is introduced from the channel inlet. Therefore, all morphological adjustments occurred after the dam breaks are driven by the difference in water surface elevation upstream and downstream of the dam.

	$D_{s1} = 1.095mm$	$D_{s2} = 2.121mm$	$D_{s3} = 4.242mm$	$D_{s4} = 7.745mm$	
$Texture$	F_1	F_2	F_3	F_4	$D_g(mm)$
T1	0.05	0.05	0.20	0.7	5.837
T2	0.20	0.78	0.02	0.0	1.884

Table 4: Grain size distributions used in the two numerical experiments.

Figures 10 and 11 present the evolution of the bed elevation and the finest grain fraction respectively (corresponding to $D_{s1} = 1.095$ mm and representing 20% and 5% of the mixtures T1 and T2). Left and right panels in each Figure represent the homogeneous and heterogeneous initial surface textures, respectively.

Figure 10 shows different bed elevation patterns depending on the initial grain size distribution of the surface (Figure 9). A deeper scour hole around the corner where channel expands to the left is observed when an heterogeneous initial bed surface is considered. By mass conservation, the depositional zone extending from the upper left corner to the lower right corner within the expansion zone is larger when the initial surface texture is composed of two different grain sizes. The finer sediment mixture along the upstream channel, intrinsically more mobile than the coarse mixture, is mainly responsible for the increase in the scour hole. The higher mobility of the finest grain texture is presented in Figure 11, in which the finest grain class, associated with $D_{s1} = 1.095$ mm is taken as a proxy. This figure shows how this grain size is washed away over the expansion when the incoming channel is composed of a finer mixture (right panels). On the contrary, when the entire domain is composed of a coarse mixture (left panels), the finest fractions only are present in the uppermost region of the depositional zone.

The grain size distribution of the surface can be summarized by the geometric mean diameter, D_g. Figure 12, which illustrates the spatial distribution of D_g for the two initial conditions outlined in Figure 9, confirms the results

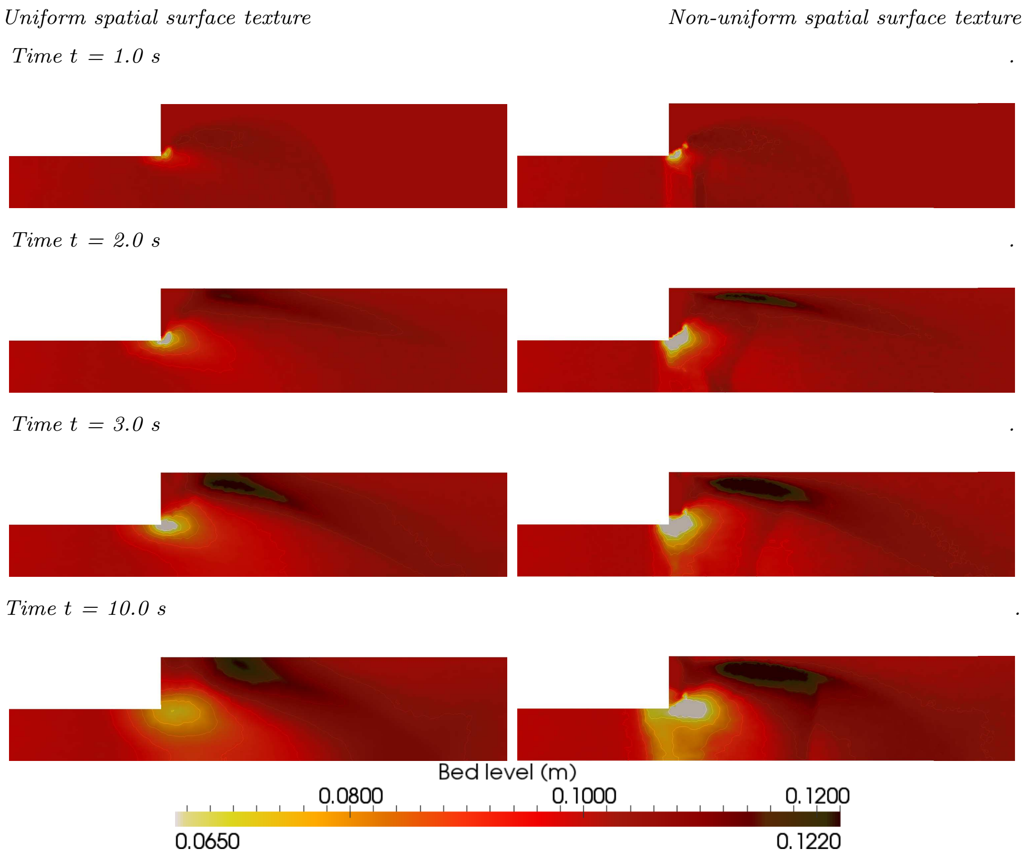

Figure 10: Spatial distribution of the bed elevation at times t = 1.0, 2.0, 3.0 and 10.0 s. Left and right figures illustrate the results obtained with a uniformly and non-uniformly distributed initial surface texture, i.e. Case DB-1 and Case DB-2.

presented in Figure 11. The finer material initially placed along the incoming channel (texture T1) is transported down to the expansion area contributing to the fining of this area in case DB-2 (non-uniform initial texture) (Figure 12 right). This material is transported as a convection-like perturbation across the wider section of the domain. Downstream of the edge of the wave of fine sediment that is translated across the expansion section, an elongated patch of coarse material expands. As time passes after the dam break, the patch size increases. This material is likely to have been dragged by the wave of fine material transported from the upstream narrow channel. The last surface distribution obtained at $t = 10$ s illustrates a decline in the extension of the coarse patch. This figure seems to show that the coarse material is likely

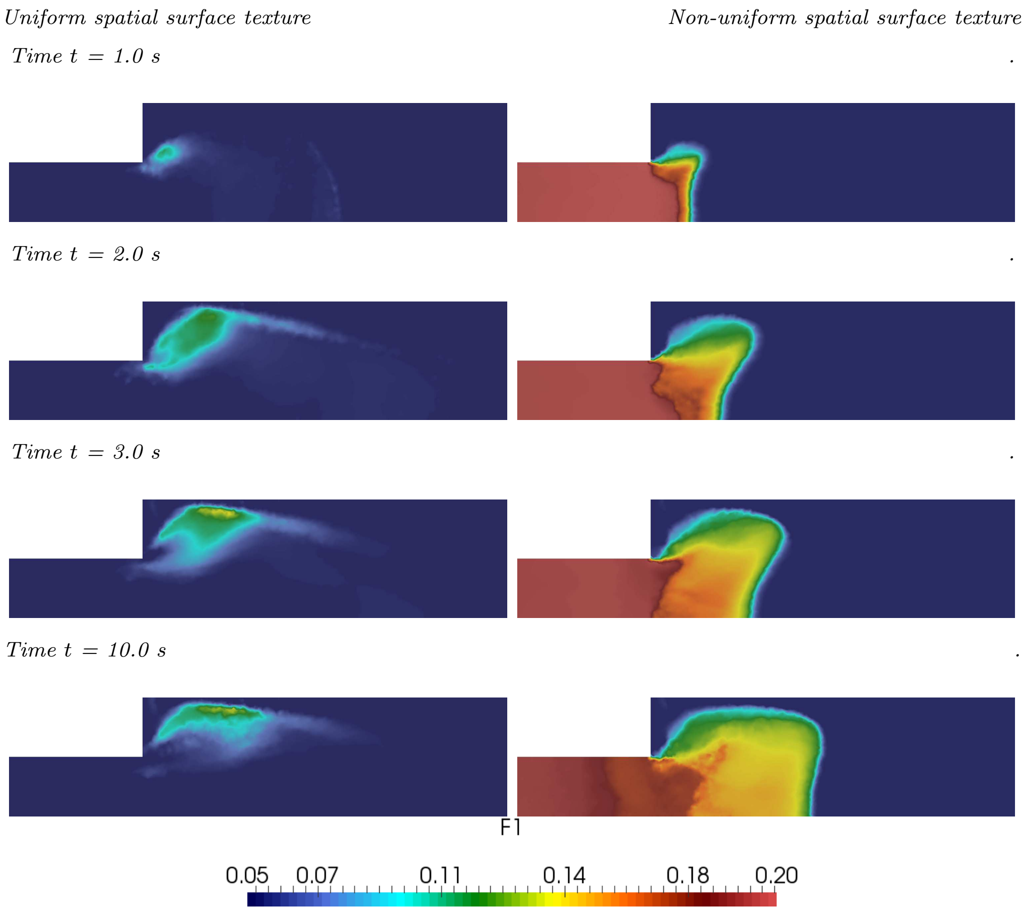

Figure 11: Spatial distribution of the finest fraction F1 at times t = 1.0, 2.0, 3.0 and 10.0 s. Left and right figures illustrate the results obtained with a uniformly and non-uniformly distributed initial surface texture, i.e. Case DB-1 and Case DB-2.

to have been buried by the fine sediment transported from the upstream narrow channel. However, since the numerical model does not store the vertical stratigraphy of the bed, this point cannot be fully demonstrated. Left panels of the Figures 12 show the spatial distribution of D_g when the uniform texture T2 extends throughout the domain (Figure 9). Two major features are noticeable from these plots: (i) the coarsening of the area around the sudden expansion and (ii) the fining of the upper zone of the expansion area. These two zones are well correlated with the areas where degradation and aggradation take place respectively (Figures 10). The finer fractions of material entrained from the degradation areas are transported and deposited

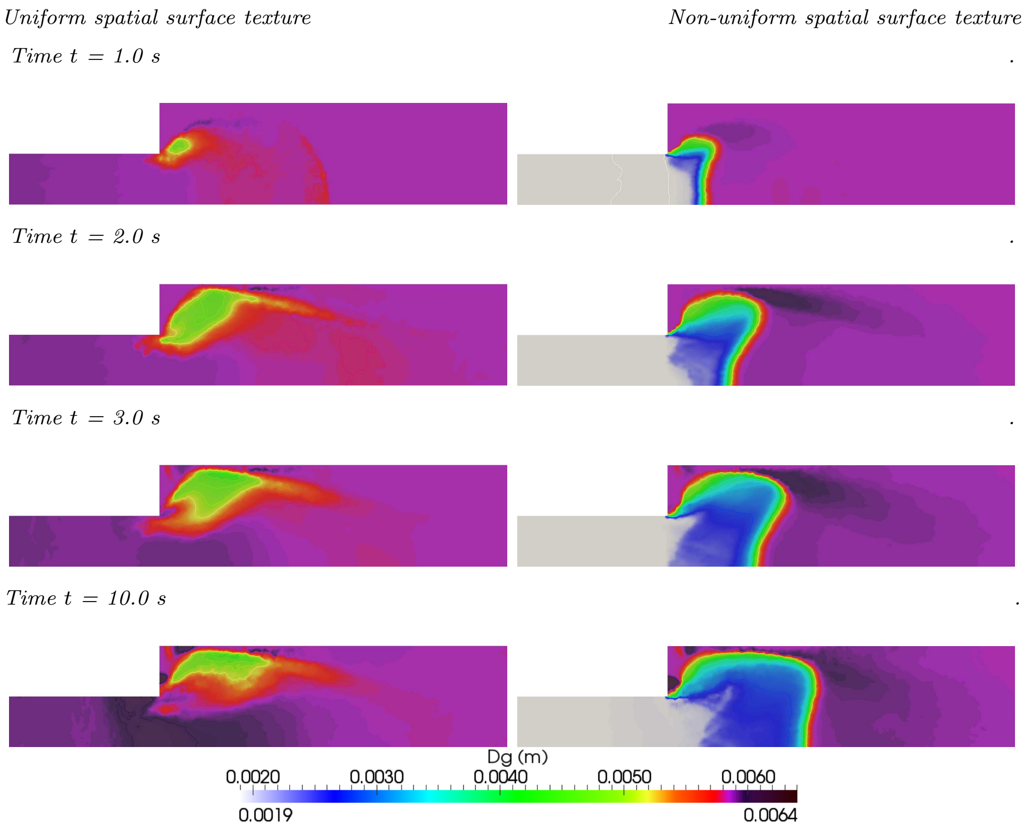

Figure 12: Spatial distribution of the mean geometric diameter at times t = 1.0, 2.0, 3.0 and 10.0 s. Left and right and considering the same grain size distribution within all the channel (left) and with a different spatial grain size distribution (right)

on the areas where the bed aggrades. Figure 12 presents the expected results as far as the evolution of D_g are concerned.
Results presented in Figure 11 show how different and significant channel adjustments are driven by changes in the spatial distribution of the surface texture. It is worth noting that in the both numerical experiments, the shape of the scour hole and the depositional zone is qualitatively the same as the one formed when the sediment of the bed is composed of uniform sediment [59].
The influence of sediment mixtures on the bed surface in highly rapid and variable flows such as dam breaks, is shown in Figure 13. This figure illustrates the bed elevation after dam break in which a uniformly distributed material expands throughout the domain. However, unlike the simulation

Case DB-1, where the initial distribution was a sediment mixture of four different grain classes (Table 4), this material is composed of only one grain size of $D = 5.837\ mm$, i.e. equal to D_g in the simulation Case DB-1. All other parameters of the numerical experiment are the same as the ones previously used. Thus, Figure 13 needs to be compared with the left-hand side panels of Figure 10. Results at $t = 2\ s$ and $10\ s$ are shown in Figure 13. Changes in the bed elevation when a uniform material is used as initial surface texture are less pronounced than when a sediment mixture is considered (Figure 10): less erosion and less aggradation are noticed with uniform sediment. This response arises from the lack of hiding/exposure effects when the material is uniform. An increase of sediment transport rates occurs when a sediment of mixture is considered. This occurs because of the presence of fine grain particles on the bed. This fine material, inherently more mobile than the coarse fractions, enhances the mobility of the coarse material, increasing bedload transport rates [60]. These effects are taken into account by the hiding/exposure function, which when the bed surface is composed of multiple grain sizes, affects the critical shear stress for the initiation of motion for each grain size. Figure 13 demonstrates the importance of considering multiple grain sizes as far as river morphodynamics are concerned.

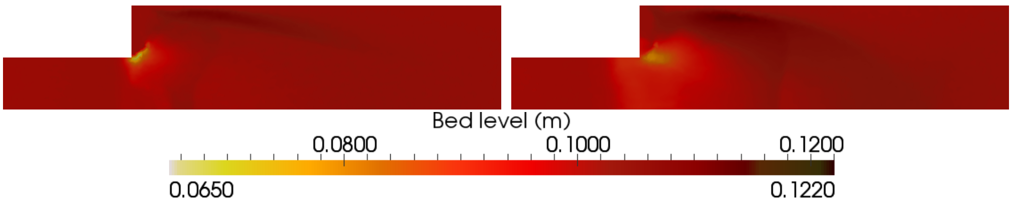

Figure 13: Bed level evolution at times $t = 2.0$ (left) and 10.0 s (right) using Ashida-Michue formula and considering uniform grain size with D_s=5.837 mm

4.3. Comparison with experiments: Dam removal

The last set of comparisons of the numerical model is carried out by testing its performance against some experiments on dam removal. The bed was composed of a poorly sorted mixture ($D_g = 3.39\ mm$, $\sigma_g = 1.8$). The dam was composed of three slats of 4 cm each that were sequentially removed. Thus, the total height of the dam was 12 cm. After the dam was removed, a channel was formed within the upstream deposit. This channel rapidly eroded and the erosions migrated upstream. The width of the upstream eroding channel narrowed during rapid stages of bed degradation and slowly widened once bed degradation rates decreased. The experiment used in this test compares the channel evolution (elevation and width). Water discharge was set constant to 0.002 m^3/s. The experiment was conducted under no feed conditions. These experiments are particularly useful for the purpose of testing the numerical model because: (i) the bed surface was composed of a mixture of sediment, (ii) flow was supercritical, bed changes were produced very rapidly (thus, significant gradients in the computed variables are expected) and (iii) channel width changes introduce important two dimensional processes. The experimental results presented herein represent the evolution of the channel after the second slat is removed. More details of the experiments can be found in [38]. An unstructured mesh with a cell size of $0.01m^2$ has been considered and the CFL has been imposed equal to 0.5. Figure 14 illustrates the evolution of the bed elevation along the center of the channel at four different times during the run. The numerical model underpredicts the erosion observed during the experiment, i.e. the erosion along the channel progresses upstream faster in the experiments than it is predicted by the numerical model. This might be due to an underprediction of the sediment transport rate, given by the Ashida-Michiue formula, that leads to an excess of surface bed coarsening that ends up limiting channel erosion.

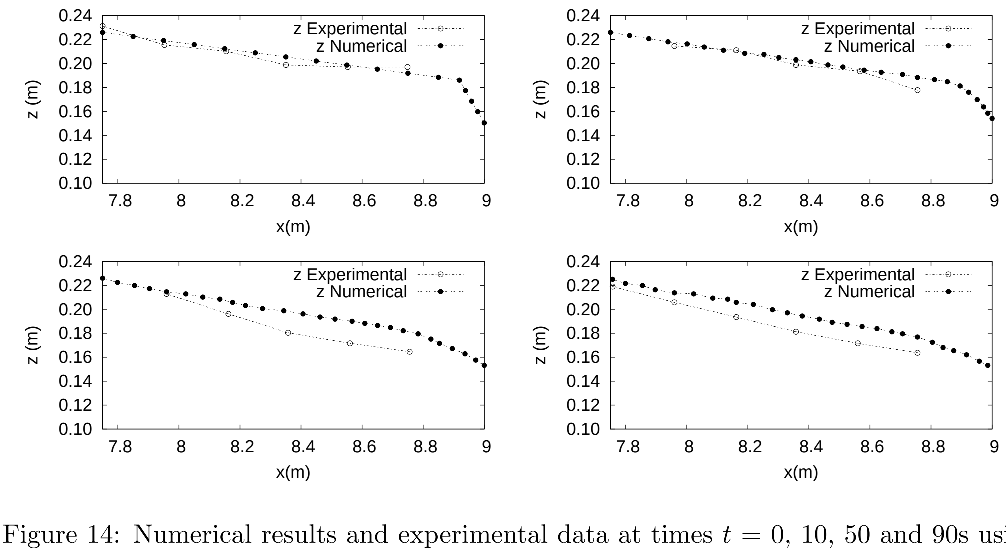

Figure 14: Numerical results and experimental data at times t = 0, 10, 50 and 90s using Ashida-Michue: measured bed level surface and computed bed level surface

Figure 15 shows the evolution of the channel width at three stations along the channel. Numerical results nicely reproduce the complex two-dimensional evolution of the channel width: magnitude and timing of the narrowing and widening of the cross-sections are well modelled. The final width of the channel at the end of the experiment is also reproduced. The numerical model does not account for sudden slides and slumps. This is the reason that the sudden increases of the channel width, caused by lateral mass movement from the sidewalls, cannot be reproduced [38].

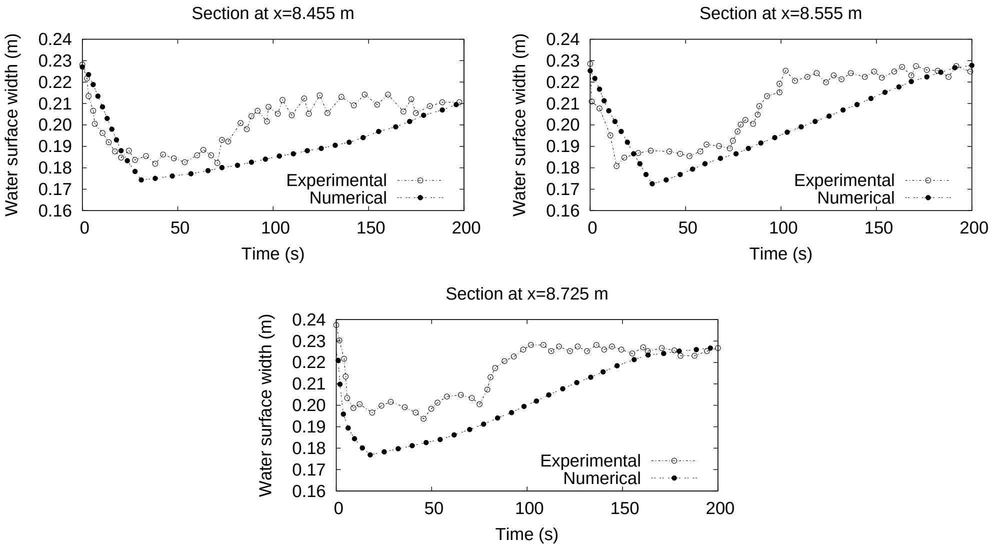

Figure 15: Numerical results and experimental data at times t = 0, 10, 50 and 90s using Ashida-Michiue formula: measured water surface width and computed water surface width

No surface samples were extracted from the bed during the experiment. However, given the characteristics of the experiments (strong degradation, constant discharge and no sediment feed), some surface coarsening is expected. Figure 16 presents the expected results: (i) surface texture coarsens, (ii) the farther upstream the station from the dam the higher the coarsening and (iii) the longer it takes to start coarsening. The mean geometric diameter D_g is coarsened in both stations as bed degradation proceeds. The station which is located farther from the dam (x=7.6 m) suffers a bigger coarsening process. This arises because upstream, bed degradation rates decrease with time. Hence, the finest grain sizes of the surface are winnowed while the coarsest fractions remain in place. This finest material is transported downstream, causing a smaller coarsening process at station x=8.0 m. Results presented in Figure 16 follow a similar trend as other numerical predictions of the experiment [38] and they are in agreement with channel bed coarsening after dam removal observed in field cases [61, 62].

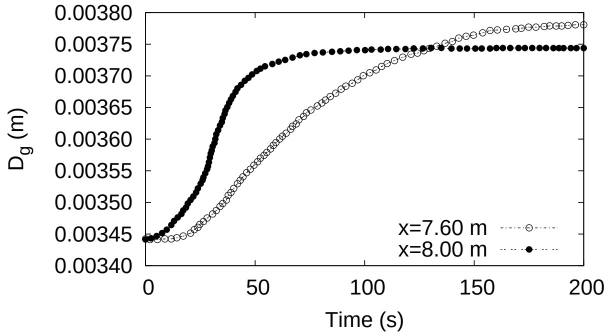

Figure 16: Numerical results of the temporal evolution of the geometric mean diameter at two stations located in the centre of the incising channel.

5. Conclusions

A novel two-dimensional numerical finite volume scheme for water flows over erodible beds considering non-uniform grain sizes has been developed. The numerical model includes the Shallow water equations to describe the flow field with the Exner equation for the bed evolution and the Hirano equations to describe the surface grain size distributions by means of a weak-coupled strategy. Thanks to this methodology, a self-stable explicit scheme is developed and no tuning parameters are required for controlling the stability of the model by means of the CFL condition.

The first test cases considered for evaluating the model are based on synthetic aggradation/degradation test cases. These test cases are useful for verifying the correct integration of the fluxes in order to obtain a final equilibrium stage. The numerical model is able to gradually achieve new equilibrium conditions once the initial configuration is disturbed. Successful results are obtained regardless of whether this new equilibrium condition is achieved through an aggradational or degradational transient process.

The second test case considered is a genuinely 2D transient problem where the computed variables display large gradients. The key point is the presence of a sudden enlargement which causes an notable local scour and sediment deposition downwards in the expanded area. Several initial texture conditions have been considered and the numerical scheme has provided self-stable results for the flow, bed level and the sediment fractions on the bed surface. Significant differences are observed in the results depending on whether the initial surface is composed of uniform material or a sediment mixture. These results evidence the importance of mixtures in river morphodynamics.

Lastly, the numerical model is compared with a set of experiments on dam removal. The numerical model is able to predict the general trend of degradation, changes in channel width and surface adjustments observed during the experiment.

6. Acknowledgments

The participation of C. Ferrer-Boix in this research was made possible in part by support from the Spanish Ministry of Education, programme "Campus de Excelencia Internacional CEI Iberus". Additionally, this work was partially supported and funded by the Spanish Ministry of Science and Technology under research project CGL2011-28590 and by Diputación General de Aragón, DGA, through FEDER funds.

References

[1] Cunge, J., Holly, F., Vervey, A.. Practical Aspects of Computational River Hydraulics. Pitman: London; 1980.

[2] Kalinske, A.. Movement of sediment as bed load in rivers. Trans AGU 1947;28:615–620.

[3] Garegnani, G., Rosatti, G., Bonaventura, L.. On the range of validity of the Exner-based models for mobile-bed river flow simulations. Journal of Hydraulic Research 2013;51(4):380–391.

[4] Cao, Z., Day, R., Egashira, S.. Coupled and decoupled numerical modeling of flow and morphological evolution in alluvial rivers. Journal of Hydraulic Engineering 2002;128:306–321. doi:10.1061/(ASCE)0733-9429(2002)128:3(306).

[5] Abderrezzak, K.K., Paquier, A.. Applicability of Sediment Transport Capacity Formulas to Dam-Break Flows over Movable Beds. Journal of Hydraulic Engineering 2011;137:209–221. doi:10.1061/(ASCE)HY.1943-7900.0000298.

[6] Castro Diaz, M., Fernandez Nieto, E., Ferreiro, A.. Sediment transport models in shallow water equations and numerical approach by high order finite volume methods. Journal of Computational Fluids 2008;37:299–316. doi:10.1016/j.compfluid.2007.07.017.

[7] Goutière, L., Soares-Frazao, S., Savary, C., Laraichi, T., Zech, Y.. One-dimensional model for transient flows involving bed-load sediment transport and changes in flow regimes. Journal of Hydraulic Engineering 2008;134(6):726–735. doi:10.1061/(ASCE)0733-9429(2008)134:6(726).

[8] Canestrelli, A., Dumbser, M., Siviglia, A., Toro, E.. Well-balanced high-order centred schemes on unstructured meshes for shallow water equations with fixed and mobile bed. Advances in Water Resources 2010;33:291–303. doi:10.1016/j.advwatres.2009.12.006.

[9] Murillo, J., García-Navarro, P.. An Exner-based coupled model for two-dimensional transient flow over erodible bed. Journal of Computational Physics 2010;229:8704–8732. doi:10.1016/j.jcp.2010.08.006.

[10] Goutière, L., Soares-Frazao, S., Zech, Y.. Dam-break flow on mobile bed in abruptly widening channel: experimental data. Journal of Hydraulic Research 2011;49(3):367–371. doi:10.1080/00221686.2010.548969.

[11] Canelas, R., Murillo, J., Ferreira, R.M.L.. Two-dimensional depth-averaged modelling of dambreak flows over mobile beds. Journal of Hydraulic Research 2013;51(4):392–407. doi:10.1080/00221686.2013.798891.

[12] Siviglia, A., Stecca, G., Vanzo, D., Zolezzi, G., Toro, E., Tubino, M.. Numerical modelling of two-dimensional morphodynamics with applications to river bars and bifurcations. Advances in Water Resources 2013;52:243–260. doi:dx.doi.org/10.1016/j.advwatres.2012.11.010.

[13] Michoski, C., Dawson, C., Mirabito, E., Kubatko, E., Wirasaet, D., Westerink, J.. Fully coupled methods for multhiphase morphodynamics. Advances in Water Resources 2013;110:59–95. doi:10.1016/j.advwatres.2013.05.002.

[14] Juez, C., Murillo, J., García-Navarro, P.. A 2D weakly-coupled and efficient numerical model for transient shallow flow and movable bed. Advances in Water Resources 2014;71:93–109. doi:10.1016/j.advwatres.2014.05.014.

[15] Wu, W.. Depth-Averaged Two-Dimensional Numerical Modeling of Unsteady Flow and Nonuniform Sediment Transport in Open Channels. Journal of Hydraulic Engineering 2004;130(10):1013–1024.

[16] Xia, J., Lin, B., Falconer, R., Wang, G.. Modelling Dam-break Flows over Mobile Beds using a 2D Coupled Approach. Advances in Water Resources 2010;33:171–183. doi:10.1016/j.advwatres.2009.11.004.

[17] Xiao, Y., Wang, H., Shao, X.. 2D numerical modeling of grain-sorting processes and grain size distributions. Journal of Hydro-environment Research 2014;8(4):452 – 458. doi:http://dx.doi.org/10.1016/j.jher.2013.08.002.

[18] Zhou, G., Wang, H., Shao, X., Jia, D.. Numerical Model for Sediment Transport and Bed Degradation in the Yangtze River Channel Down-

stream of Three Gorges Reservoir. Journal of Hydraulic Engineering 2009;135(9):729–740. doi:10.1061/(ASCE)0733-9429(2009)135:9(729).

[19] Sun, J., Binliang, L., Yang, H.. Development and application of a braided river model with non-uniform sediment transport . Advances in Water Resources 2015;(45):1100–1115 . doi:10.1016/j.advwatres.2014.12.012.

[20] Parker, G.. Sediment inertia as cause of river antidunes. Journal of Hydraulic Engineering 1975;101:211–221.

[21] Wu, W.. Computational river dynamics. Taylor and Francis; 2007.

[22] Wang, G., Xia, J., Wu, B.. Numerical Simulation of Longitudinal and Lateral Channel Deformations in the Braided Reach of the Lower Yellow River. Journal of Hydraulic Engineering 2008;134(8):1064–1078. doi:10.1061/(ASCE)0733-9429(2008)134:8(1064).

[23] Blom, A., Ribberink, J., Parker, G.. Vertical sorting and the morphodynamics of bed form-dominated rivers: a sorting evolution model. Journal of Geophysical Research 2008;113:F01019. doi:10.1029/2006JF000618.

[24] Hirano, M.. River bed degradation with armoring. Trans Jpn Soc Civ Eng 1971;3:194–195.

[25] Parker, G.. Transport of Gravel and Sediment Mixtures. In: Garcia, M.H., editor. Sedimentation Engineering. Processes, measurements, modeling and practice; chap. 3. ASCE, Reston, VA.; 2008, p. 165–251.

[26] Parker, G., Klingeman, P.. On why gravel bed streams are paved. Water Resources Research 1982;18(5):1409–1423.

[27] Parker, G.. Surface bedload transport relation for gravel rivers. Journal of Hydraulic Research 1990;28(4):417–436.

[28] Wilcock, P.R., Crowe, J.C.. Surface-based Tranport Model for Mixed-Size Sediment. Journal of Hydraulic Engineering 2003;129(2):120–128. doi:10.1061/(ASCE)0733-9429(2003)129:2(120).

[29] Stecca, G., Siviglia, A., Bom, A.. Mathematical analysis of the Saint-Venant-Hirano model for mixed-sediment morphodynamics. Water Resources Research 2014;52:7563–7589. doi:10.1002/2014WR015251.

[30] Hoey, T.B., Ferguson, R.. Numerical simulation of downstream fining by selective transport in gravel bed rivers: Model development and illustration. Water Resources Research 1994;30:128–129. doi:10.1029/94WR00556.

[31] Cui, Y., Parker, G., Pizzuto, J.E., Lisle, T.E.. Sediment pulses in mountain rivers: 1. Comparison between experiments and numerical predictions. Water Resources Research 2003;39(9):1240. doi:10.1029/2002WR001805.

[32] Cui, Y., Parker, G.. Numerical model of sediment pulses and supply disturbances in mountain rivers. Journal of Hydraulic Engineering 2005;131(8):646–656.

[33] Cui, Y., Parker, G., Braudrick, C., Dietrich, W.E., Cluer, B.. Dam Removal Express Assessment Models (DREAM). Part 1: Model development and validation. Journal of Hydraulic Research 2006;44(3):291–307.

[34] Viparelli, E., Sequeiros, O.E., Cantelli, P.R., Wilcock, P.R., Parker, G.. River morphodynamics with creation/consumption of grain size stratigraphy 2: numerical model. Journal of Hydraulic Research 2010;46(6):726–741.

[35] De Almeida, G., Rodríguez, J.F.. Understanding pool-riffle dynamics through continuous morphological simulations. Water Resources Research 2011;47(1):n/a–n/a. doi:10.1029/2010WR009170.

[36] Viparelli, E., Gaeuman, D., Wilcock, P.R., Parker, G.. A model to predict the evolution of a gravel bed river under an imposed cyclic hydrograph and its application to the Trinity River. Water Resources Research 2011;47:W02533. doi:10.1029/2010WR009164.

[37] Viparelli, E., Blom, A., Ferrer-Boix, C., Kuprenas, R.. Comparison between experimental and numerical stratigraphy emplaced by prograding bedforms with a downstream slip face. Earth Surface Dynamics 2014;1:1–36. doi:10.5194/esurfd-1-1-2014.

[38] Ferrer-Boix, C., Martín-Vide, J.P., Parker, G.. Channel evolution after dam removal in a poorly sorted sediment mixture: Experiments and numerical model. Water Resources Research 2014;50(11):89970–879019. doi:10.1002/2014WR015550.

[39] Ferrer-Boix, C., Hassan, M.A.. Influence of the sediment supply texture on morphological adjustments in gravel-bed rivers. Water Resources Research 2014;50(11):88680–878890. doi:10.1002/2013WR015117.

[40] De Vriend, H., Zyserman, J., Nicholson, J., Roelvink, J., Pechon, P., Southgate, H.. Medium-term 2DH coastal area modelling. Journal of Coastal Engineering 1993;21:193–224. doi:10.1016/0378-3839(93)90050-I.

[41] Ribberink, J.S.. Mathematical modeling of one-dimensional morphological changes in rivers with non-uniform sediment. PhD Thesis at Delft University 1987;-:Netherlands.

[42] Sieben, J.. Modelling of hydraulics and morphology in mountain rivers. PhD Thesis 1997;Delft University of Technology:Delft, Netherlands.

[43] Toro, E.. Shock-Capturing Methods for Free-Surface Shallow Flows. Wiley, New York; 2001.

[44] Parker, G.. Selective sorting and abrasion of river gravel. Part I. Theory. Journal of Hydraulic Engineering 1991;117:113–149.

[45] Stecca, G., Siviglia, A., Bom, A.. An accurate numerical solution to the Saint-Venant-Hirano model for mixed-sediment morphodynamics in rivers. Advances in Water Resources Research 2015;In press:–. doi:10.1016/j.advwatres.2015.05.022.

[46] Hirano, M.. Studies on variation and equilibrium state of a river bed composed of nonuniform material. Trans Jpn Soc Civ Eng 1971;4:128–129.

[47] Toro-Escobar, C.M., Parker, G., Paola, C.. Transfer function for the deposition of poorly sorted gravel in response to streambed aggradation. Journal of Hydraulic Research 1996;34(1):35–53.

[48] Cordier, S., Le, M., Morales de Luna, T.. Bedload transport in shallow water models: Why splitting (may) fail, how hyperbolicity (can) help. Advances in Water Resources 2011;34:980–989. doi:10.1016/j.advwatres.2011.05.002.

[49] Manning, R.. On the flow of water in open channels and pipes. Transactions of the Institution of Civil Engineers of Ireland 1895;20:161–207.

[50] Einstein, H.. The bed-load function for sediment transportation in open channel flows. Tech. Rep; 1950.

[51] Meyer-Peter, E., Müller, R.. In: Report on the 2nd Meeting International Association Hydraulic Structure Research. Stockholm, Sweden; 1948.

[52] Smart, G.. Sediment transport formula for steep channels. Journal of Hydraulic Engineering 1984;3:267–276.

[53] Camenen, B., Larson, M.. A general formula for non-cohesive bed load sediment transport. Estuarine, Coastal and Shelf Science 2005;63:249–260. doi:10.1016/j.ecss.2004.10.019.

[54] Ashida, K., Michiue, M.. Study on hydraulic resistance and bedload transport rate in alluvial streams. Transactions, Japan Soc Civil Eng 1972;206:569–589.

[55] Eguiazarov, I.. Calculation of non-uniform sediment concentrations. Journal of Hydraulic Engineering 1965;91(4):225–248.

[56] Murillo, J., García-Navarro, P.. Weak solutions for partial differential equations with source terms: Application to the shallow water equations. Journal of Computational Physics 2010;229:4327–4368. doi:10.1016/j.jcp.2010.02.016.

[57] Parker, G., Paola, C., Leclair, S.. Probabilistic Exner sediment continuity equation for mixtures with no active layer. Journal of Hydraulic Engineering 2000;126(11):818–826.

[58] Parker, G., Wilcock, P.. Sediment feed and recirculating flumes: fundamental difference. Journal of Hydraulic Engineering 1993;119(11):1192–1204.

[59] Soares-Frazao, S., Canelas, R., Cao, Z., Cea, L., Chaudhry, H., Moran, A., et al. Dam-break flows over mobile beds: experiments and benchmark tests for numerical models. Journal of Hydraulic Research 2012;50:4:364–375. doi:10.1080/00221686.2012.689682.

[60] Curran, J.C., Wilcock, P.R.. Effect of Sand Supply on Transport Rates in a Gravel-Bed Channel. Journal of Hydraulic Engineering 2005;131(11):961–967.

[61] Burroughs, B., Hayes, D.B., Klomp, K.D., Hansen, J.F., Mistak, J.. Effects of Strobach Dam removal on fluvial geomorphology in the Pine River, Michigan, United States. Geomorphology 2009;110(3–4):96–107. doi:10.1016/j.geomorph.2009.03.019.

[62] Pearson, A.J., Snyder, N.P., Collins, M.J.. Rates and processes of channel response to dam removal with a sand-filled impoundment. Water Resources Research 2011;47:W08504. doi:10.1029/2010WR009733.